Characterizing Non-phase-locked Tidal Currents in the California Current System using High-frequency Radar

Luke Kachelein[1,2], Sarah T. Gille[1], Matthew R. Mazloff[1], and Bruce D. Cornuelle[1]

[1]Scripps Institution of Oceanography, University of California San Diego, La Jolla, CA, United States
[2]Jet Propulsion Laboratory, California Institute of Technology, Pasadena, CA, United States

Key Points:

- In the California Current System, High-Frequency Radar resolves stationary and non-stationary tides.
- Broadband cusps occur at tidal constituent frequencies, with M2 exhibiting annual modulation.
- We analyze the tidal modulation to assess physics governing non-stationary tidal variability.

Corresponding author: Luke Kachelein, lkachele@ucsd.edu or luke.kachelein@jpl.nasa.gov,

Abstract

Over nine years of hourly surface current data from high-frequency radar (HFR) off the US West Coast are analyzed using a Bayesian least-squares fit for tidal components. The spatial resolution and geographic extent of HFR data allow us to assess the spatial structure of the non-phase-locked component of the tide. In the frequency domain, the record length and sampling rate allow resolution of discrete tidal lines corresponding to well-known constituents and the near-tidal broadband elevated continuum resulting from amplitude and phase modulation of the tides, known as cusps. The FES2014 tide model is used to remove the barotropic component of tidal surface currents in order to evaluate its contribution to the phase-locked variance and spatial structure. The mean time scale of modulation is 243 days for the M_2 constituent and 181 days for S_2, with overlap in their range of values. These constituents' modulated amplitudes are significantly correlated in several regions, suggesting shared forcing mechanisms. Within the frequency band $M_2 \pm 5$ cycles per year, an average of 48% of energy is not at the phase-locked frequency. When we remove the barotropic model, this increases to 64%. In both cases there is substantial regional variability. This indicates that a large fraction of tidal energy is not easily predicted (e.g. for satellite altimeter applications). The spatial autocorrelation of the non-phase-locked variance fraction drops to zero by 150 km, comparable to the width of the swath of the recently launched Surface Water and Ocean Topography (SWOT) altimeter.

Plain Language Summary

Tides in the ocean encompass both the highly predictable daily changes in sea level seen from the shore as well as a less predictable component that changes over time depending on seasonal conditions and wind. Tidal signals are visible to instruments that observe the surface of the ocean, including satellites and land-based radar antennas. The time-evolving tide signals interact with other processes in the ocean, like currents, and can become harder to predict and describe. Many studies have examined this aspect of tides. In this work, we use land-based radar observations of ocean currents off the US West Coast to examine this process with high detail, using mathematical techniques to separate the tides from everything else and then evaluating how much the tide has been altered by other processes. This is useful because ocean-observing satellites can observe a single part of the ocean only when the satellite passes overhead, approximately every

10 to 20 days, while the data we analyze are sampled hourly and thus more easily allow us to draw conclusions about how tides behave.

1 Introduction

Barotropic tidal currents are known to dissipate in shallow seas via bottom boundary layer drag and in the deep ocean via scattering over topography and subsequent conversion to internal tides (Baines, 1982; Munk & Wunsch, 1998; Egbert & Ray, 2000; R. D. Ray & Cartwright, 2001; Garrett & Kunze, 2007). The deep ocean conversion of barotropic to baroclinic (internal) tides accounts for 25-30% of the total barotropic energy loss and ultimately may provide roughly half of the mixing energy required to maintain the global overturning circulation (Egbert & Ray, 2000). Thus the internal tide plays an important role in the world ocean. Surface signatures of internal tides have long been detected from satellite altimetry (e.g. R. D. Ray & Mitchum, 1996), analysis of which using traditional tidal harmonic methods relies on years of observations to extract highly repeatable phase-locked signals (R. D. Ray & Zaron, 2011). However, the total energy of the internal tide has a substantial component that is not phase-locked to the astronomical forcing terms due to modulation and scattering of propagating internal tides by mesoscale processes (Mitchum & Chiswell, 2000; Chiswell, 2002; Rainville & Pinkel, 2006). Tidal signals have long been known to alias to well-defined low frequencies when sampled by satellites, the orbital periods of which are longer than tidal periods (Parke et al., 1987), and models to account for this phenomenon have been implemented R. Ray (1993). Unlike the large-scale, predictable barotropic tide, this non-phase-locked baroclinic component is difficult to remove from altimeter data and therefore poses a challenge to present and future high-spatial-resolution satellite missions, as it can contaminate mesoscale and submesoscale signals (Chavanne & Klein, 2010; Savage, Arbic, Alford, et al., 2017; Zaron & Ray, 2018). Due to its relevance for detiding altimetry and for assessing ocean mixing, the non-phase-locked tide has been a widely investigated topic, both observationally and computationally (e.g. R. D. Ray & Zaron, 2011; Ponte & Klein, 2015; Zaron, 2015; Dunphy et al., 2017; Huang et al., 2018; Savage et al., 2020), with the non-phase-locked tide estimated and mapped at a global scale, both from satellite altimetry (Zaron, 2017) and from output from HYCOM, a global ocean general circulation model (Shriver et al., 2014; Savage, Arbic, Richman, et al., 2017; Nelson et al., 2019). Although model-guided estimation of this tidal component has been demonstrated at a regional scale (Eg-

bert & Erofeeva, 2021), a regional study of the spatial structure of the non-phase-locked tide using observations with high spatial and temporal resolution has not been conducted to our knowledge. Fully characterizing this component observationally can help validate numerical studies and ultimately provide critical information needed to assess tidal variability in newer high-resolution satellite missions, such as the recently-launched Surface Water and Ocean Topography (SWOT) mission, which aims to resolve sea surface height at 15-30 km wavelengths (Morrow et al., 2019).

The goals of this study are to use high-frequency radar (HFR) measurements of surface currents to quantify the non-phase-locked tide. HFR-derived surface currents are a valuable source of spatially high-resolution, decade-long hourly observations (Terrill et al., 2006), and could therefore prove useful for characterizing non-phase-locked tidal variability and spatial scale. The U.S. Integrated Ocean Observing System (IOOS) High Frequency Radar Network (HFRNet) is one of many national networks that comprise the Global HFR Network (Roarty et al., 2019). HFRNet differentiates observation sites by region, with the United States West Coast (USWC) array providing over a decade of publicly available data spanning the Pacific Coast of North America from the U.S.-Mexico border to the mouth of the Columbia River. HFR surface currents have been used to study coastal jets, eddies, near-inertial motions, and tidal currents, from the submesoscale to the mesoscale (e.g. Erofeeva et al., 2003; Kurapov et al., 2003; Kosro, 2005; Chavanne & Klein, 2010; Kim et al., 2010, 2011; Kim & Kosro, 2013); however, these studies did not do detailed analysis of the non-phase-locked tide.

In order to characterize the non-phase-locked tide in the California Current System (CCS), we examine USWC HFR data using the red_tide harmonic analysis package, which uses a Bayesian approach that accounts for spectrally red background energy and allows for tidal cusps (Kachelein et al., 2022). We then compare our analysis with a barotropic tidal model and further partition the tidal signal into baroclinic and barotropic components in order to investigate the share of non-phase-locked energy that remains after removing the barotropic component, which is more coherent with astronomical forcing and is typically removed when analyzing altimeter observations (Chavanne & Klein, 2010) or when describing the non-phase-locked tide (e.g. R. D. Ray & Zaron, 2011; Wang et al., 2018). We also compare the modulation of the amplitude of M_2 and S_2 currents in order to evaluate the processes that lead to modulation.

This study uses USWC HFRNet observations to quantify the degree to which regional tidal surface currents are non-phase-locked. We build upon previous studies that investigate this problem on a global scale at lower spatial resolution. We begin with an overview of the data and model in this region (Section 2), followed by a brief description of the tidal analysis package and an overview of tidal modulation (Section 3). We then present results of this analysis, including the spatial structure and amplitude of non-phase-locked tidal currents, the time scales of their modulation, and a comparison of the modulation of the M_2 and S_2 constituents (Section 4), and we end with a discussion of these results (Section 5) and conclusions in the context of future work and the implications of our analysis for satellite altimeter and scatterometer missions (Section 6).

1.1 Defining the Non-Phase-Locked Tide

Tides can be subdivided into "phase-locked" and "non-phase-locked" components. The "phase locked" portion of the tide is usually associated with the barotropic tide, meaning that it depends largely on ocean depth and is highly regular such that it can be readily predicted and removed. The non-phase-locked component of the tide has an amplitude and phase that vary in time due to interactions of internal tides propagating through a varying medium. The interaction of tides with non-tidal processes leads to so-called tidal cusps in the frequency domain (Munk et al., 1965; Radok et al., 1967; Matte et al., 2013), continuous prominences of spectral power which encompass a range of frequencies centered on tidal forcing frequencies. This feature is common to tidal peaks and is not an artifact of spectral analysis techniques. Though we refer to this variable tide as the non-phase-locked tide, we interpret it in the frequency domain as a non-*frequency*-locked signal at near-tidal, but not exactly tidal, frequencies. This is because the astronomical forcing is assumed to occur at exactly the known tidal frequencies for the purposes of this study.

The non-phase-locked tidal variance is not a standardized quantity, and is often calculated as the difference in spectral power before and after the removal of the phase-locked tide, usually via a least squares fit (Nelson et al., 2019). For example, in their analysis of Topex/Poseidon and Jason satellite altimeter data, R. D. Ray & Zaron (2011) calculated the non-phase-locked tidal energy as the difference between the wavenumber spectra of sea surface height (SSH) along a ground track before and after removal of 12 major tidal constituents via point by point harmonic analysis, within the bands of mode-

1 and mode-2 semidiurnal wavenumbers. Similarly, Savage et al. (2020) analyzed moored data and semi-idealized internal tide model output and calculated the total tidal component by bandpass filtering time series around the M_2 constituent frequency $\omega_{M_2} \pm 0.4$ cpd, which they then separate into phase-locked and non-phase-locked components via least squares fits to the M_2 and S_2 harmonics.

2 Data

2.1 High-Frequency Radar (HFR)

HFR observations of surface currents are obtained by a land-based network of antennas that measure the radio signal backscattered off of the ocean surface. Surface velocities are inferred using a multiple signal classification (MUSIC) algorithm (Schmidt, 1986; Barrick & Lipa, 1997). The HFR National Network (Terrill et al., 2006; Roarty et al., 2019) provides archived surface ocean velocities mapped to grids at 1 km, 2 km, and 6 km spacing (Fredj et al., 2016). We examine only 6 km gridded data, which are available over nearly the entire continental US West Coast and resolve the $\mathcal{O}(10)$ km mode-1 internal semidiurnal tide while providing data from the coast out to 200 km offshore; this is farther than either the 1 km or 2 km gridded products, which also do not provide continuous coverage along the coast.

These gridded fields are produced using an unweighted least-squares fit performed on radial surface current data. For information about the fitting procedure see Lipa & Barrick (1983); Gurgel (1994). For the 6 km gridded product, the unweighted least squares fit approach is performed on radial data within a 10 km search radius centered on the grid location (Otero, 2021, personal communication), producing zonal and meridional currents, u and v, as well as the zonal and meridional geometric Dilution of Precision (DOPX and DOPY), which are measures of the uncertainty of the current estimate due to antenna geometry (U.S. Integrated Ocean Observing System, 2016). The horizontal dilution of precision (HDOP) is the sum of DOPX and DOPY; in the publicly available data set we use, data are only provided for HDOP ≤ 1.25.

Our study region extends from 32.24°N to 46.43°N and is focused on the California Current System (CCS). For quality control, we require 50% temporal coverage at each location that we analyze. This level of coverage is typically available within 100-200 km from the coast, as shown in Figure 1a. Offshore observations are limited by the locations

of antennas that comprise the observation system: gridded data quality control requires at least three radial velocity observations from at least two antennas in order to estimate velocity **u** (Otero, 2021, personal communication), as the number of radial velocity observations within a grid point's search radius and their bearing angles influence the dilution of precision (DOP) (Kim et al., 2008). Hourly data are used from 1 January 2012 through 1 April 2021. Figure 1b shows the mean flow of the surface current in this domain, which is characterized by a broadly equatorward surface current and offshore advection, consistent with drifter observations of the CCS (Centurioni et al., 2008). Figure 1c shows $\sqrt{(\sigma_u^2 + \sigma_v^2)/2}$, the square root of eddy kinetic energy. Regions with the highest values for this quantity typically fall outside our coverage threshold; it is unknown which regions of high total energy are physical or a consequence of poor DOP due to antenna placement, though the fact that high energy areas along the coast are generally limited to regions with low coverage suggests an effect of the observation network, hence our threshold.

2.2 FES2014 Barotropic Tidal Model

In order to distinguish the baroclinic tides from coherent barotropic signals, we use the 2014 version of the Finite Element Solution (FES2014) barotropic tidal model (Lyard et al., 2021) as an estimate of the barotropic component of the total tidal current. This model was designed to provide tidal elevation predictions for use with satellite altimetry data, and it also provides tidal current maps for 34 tidal constituents. FES2014 model constituent frequencies that we fit include the O_1, S_1, K_1, N_2, M_2, S_2, and K_2; however, we only compare HFR and FES2014 at the M_2, as it is the most energetic constituent. The model, which assimilates both tide gauge and satellite sea surface height data, is run on an unstructured grid. This grid improves performance near coasts and shelves. The original model output is gridded onto a $1/16°$ ($\sim$6.9 km) resolution regular grid; for this study, the phase and amplitude of the global model are mapped to the 6 km grid of the HFR data in the CCS region via bilinear interpolation. The current from FES2014 is treated as the barotropic tidal component of the total signal observed by HFR, and is assumed to occur exactly at the tidal forcing frequency. This is justified by the apparent lack of an underlying domain-wide phase coherence at near-tidal frequencies from harmonically decomposed HFR data (not shown) compared to the partially spatially-coherent phase seen at the tidal forcing frequency in HFR. The removal of the modeled

barotropic component from harmonically decomposed HFR data is outlined in the appendix.

3 Methods

3.1 Tidal Harmonic Analysis

Harmonic analysis of tides is frequently performed using ordinary least squares and sinusoidal basis functions (Foreman, 1977; Pawlowicz et al., 2002). Several software packages use modified procedures for the least squares fit, such as iteratively re-weighted least squares (Leffler & Jay, 2009), directly embedding long-period signals (Foreman et al., 2009), or incorporating non-tidal river flow (Matte et al., 2013). Some packages seek to improve and unify various methods to serve as a general tool (Codiga, 2011).

Surface currents contain signals from several sources, including the tides, wind, and low-frequency variability, and therefore are energetic across a wide range of frequencies. These HFR time series are analyzed using harmonic analysis techniques designed for non-stationary tides in the presence of spectrally colored noise, where the term "noise" is used to describe any non-tidal variability that may complicate the estimation of tidal parameters. Tidal harmonic amplitudes are given by Bayesian maximum posterior estimation assuming Gaussian linear statistics, as described by Kachelein et al. (2022). The appendix provides a brief overview of this method using modified notation following Ide et al. (1997).

3.2 Calculating the Non-Phase-Locked Tide

We define the non-phase-locked tide similarly to previous studies, but limit our scope to frequencies that are explicitly fit via equation (A.3) (see Appendix for more information). We therefore define the phase-locked component as the harmonic fit at a tidal forcing frequency f_i, the i'th element of $\mathbf{f}$; and the non-phase-locked component as the sum of the other harmonic fits within a narrow frequency band, from f_{i-N} to f_{i+N}, such that the phase-locked fraction of variance can be defined from harmonic coefficients as

$$F_{\mathrm{PL}} = \frac{a_i^2 + b_i^2 + c_i^2 + d_i^2}{\sum_{j=i-N}^{i+N}(a_j^2 + b_j^2 + c_j^2 + d_j^2)}, \tag{1}$$

where a and b are respectively the sine and cosine harmonic coefficients that comprise $\hat{\mathbf{x}}_u$, c and d are the same for $\hat{\mathbf{x}}_v$, and i is the index of the tidal frequency in question. The non-phase-locked fraction of variance is simply $F_{\mathrm{NPL}} = 1 - F_{\mathrm{PL}}$. A similar approach

for calculating both phase-locked and non-phase-locked tidal components directly from amplitudes given by a least squares fit has been used previously (e.g. Dushaw et al., 1995). However, energy at frequencies that are not explicitly included in the tidal fitting process is missed in this definition. In order to identify the full contribution of the non-phase-locked tide, the fitted harmonics should span enough frequencies in a band centered on the central tidal frequency such that most of each tidal constituent's total energy is included in the fit. The width of a cusp is related to the spectrum of the process that non-linearly forces it (Matte et al., 2013), so fitting more nearby frequencies (widening the band) will allow more near-tidal variance to be captured. Therefore we fit to the central frequency ± 5 cpy for both M_2 and S_2, which captures modulation of these constituents by processes with periods of 0.2 years and longer.

3.3 Tidal Modulation

Following Chiswell (2002), a tidally-driven, amplitude- and phase-modulated process $a(t)$ can be written

$$a(t) = A(t)\cos[2\pi f_{\text{tidal}} t + \phi(t)], \tag{2}$$

where f_{tidal} is the ordinary frequency of some tidal constituent, $A(t)$ is the time-varying amplitude, and $\phi(t)$ is the time varying phase. The frequency-domain transform of a time series with a modulated tidal component contains information about the structure of the modulation. When phase is modeled as a first-order autoregressive process with some time scale $1/\lambda$, the power spectrum of $a(t)$, assuming that amplitude is constant in time, i.e. $A(t) = A_0$, is modeled by a Lorentzian (or Cauchy) distribution plus a mean (Zaron, 2022):

$$S_a(f) = S_0 + \frac{\alpha}{\pi\lambda\left[1 + \left(\frac{f - f_{\text{tidal}}}{\lambda}\right)^2\right]}, \tag{3}$$

where α and λ are parameters that can be estimated via a non-linear least squares fit. If $A(t)$ is modeled as a first-order autoregressive process, $S_a(f)$ is also of this form via the convolution of the spectrum of a sinusoidal tide and the spectrum of $A(t)$ (von Storch & Zwiers, 2003).

We assume that all observed modulated tidal signal are baroclinic, as barotropic tides are negligibly modulated (Colosi & Munk, 2006). Tidal energy becomes non-stationary via both amplitude and phase modulation of tidal constituents. Mitchum & Chiswell (2000), for example, found that the low-frequency variability observed in both the amplitude and

phase of the M_2 constituent is correlated with low-frequency sea level variations, which in turn are correlated with stratification variations, the proposed modulation mechanism. Therefore, information about the processes that modulate tidal constituents should be recoverable from the fitted tidal harmonic coefficients. We focus on amplitude modulation by finding the time-varying amplitude (*envelope*) that modulates the higher-frequency oscillating tide (*carrier wave*).

Figure 2 shows a simplified example of tidal modulation in both the time and frequency domains. The top panel (a) shows the apparent phase and amplitude modulation of one tidal constituent by the addition of a different constituent of a similar frequency (here M_2 and S_2). This fortnightly interference pattern simulates the well-known and ubiquitous spring-neap cycle at the lunar synodic fortnightly frequency (Parker, 2007). The power spectrum of the total signal (blue, right) is comprised of two peaks at f_{M_2} and f_{S_2} while that of the recovered non-sinusoidal modulating envelope (red) has a fundamental frequency at $f_{MSf} = f_{S_2} - f_{M_2}$ with harmonics of decreasing power at integer multiples of f_{MSf}, including frequencies at which the low amplitude peaks are not plotted. The middle panels (b) show a low-frequency sinusoidal envelope (red) modulating the amplitude of a high-frequency sinusoidal carrier signal (blue) at the M_2 frequency. The frequency of the modulating envelope, f_{mod}, in (b) is set to the spring-neap frequency f_{MSf} for the sake of comparison and visual clarity (amplitude modulation as observed in HFR data is most evident on an annual cycle). In the frequency domain, the power spectrum of the envelope is a single peak at the modulating frequency f_{mod}, while the modulated time series has a power spectrum of three peaks: a higher-amplitude central peak at the carrier frequency and two lower-amplitude peaks at $f_{M_2} \pm f_{mod}$. The bottom panels (c) show the general case of amplitude modulation by a broadband process, here an AR(1) autoregressive process with coefficient 0.95 (for more information, see Chapters 10.3 and 11.2.3 of von Storch & Zwiers, 2003). The broadband envelope has a power spectrum that is centered around the carrier frequency in the power spectrum of the modulated time series. The gray power spectrum is calculated from the data as the square of the discrete Fourier transform, while the smooth blue spectrum is given by the convolution of the theoretical spectrum of the AR(1) process (red) with that of the tidal carrier wave. In both cases of amplitude modulation (b-c), the power spectrum of the envelope is centered around the line spectrum of the sinusoidal carrier wave, while

in the case of adding constituents (a), there is apparent phase and amplitude modulation that complicate the simple frequency domain convolution of envelope and carrier.

We fit the HFR data to each prominent tidal consituent: O_1, S_1, N_2, M_2, and S_2. Frequencies are fitted in a narrow band centered on the tidal frequency, spanning ± 5 cpy, and spaced by $\Delta f = 1/9$ cpy. The modulated current for any of these constituents can be viewed as a slowly-varying ellipse, whose inclination, semi-minor axis, and semi-major axis are approximately constant across a single tidal period but evolve over time. We estimate the evolution of the semi-major axis length of the fitted vector surface currents at the two major semidiurnal constituents, M_2 and S_2, in order to compare the modulation of these two independently forced constituents in a way that takes into account all four vector components. Within the latitudes of the domain, these are the major propagating constituents that we expect to be modulated by non-tidal processes, and because they are at similar frequencies, we expect them to be modulated similarly.

The semi-major axis is a physically relevant quantity that describes the maximum tidal current amplitude over a tidal period regardless of orientation and eccentricity of the current ellipse. For a single frequency component, this quantity is constant and can be calculated from the four total harmonic coefficients of u and v at that frequency, but for the evolving ellipse, which contains energy at multiple frequencies, we numerically estimate the semi-major axis length as the maximum value of $\sqrt{u_{\text{band}}^2 + v_{\text{band}}^2}$ over each integer ceiling of the tidal period in hours (i.e. 13 hour intervals for M_2 and 12 hour intervals for S_2 in order to ensure that the maximum in each cycle is sampled). The time series of this value is taken as the "semi-major axis envelope". In constructing the time series for each modulated tidal component (u_{M_2}, v_{M_2}, u_{S_2}, and v_{S_2}), we multiply the harmonic coefficients by a Hanning window 10 cpy wide and centered on the tidal frequency in order to reduce spectral leakage. The Pearson correlation coefficient of the envelopes of these two constituents is then calculated at each location in order to estimate the extent to which they are modulated by the same processes.

To estimate the time scale λ^{-1} of tidal modulation related to non-annual, low-frequency processes, whether of phase or amplitude, we fit harmonic amplitudes directly to (3) for M_2, S_2, and O_1 within windows of $\pm$ 5 cpy using the iterative Gauss-Newton algorithm (Bishop et al., 1985). Energetic peaks are manually removed so that only the cusp is fit: tidal peaks, peaks of the annual modulation, and amplitudes at frequencies correspond-

ing to modulation of 3 years or longer typically prevent the least-squares method from converging to curves with reasonable parameters. The mean and uncertainty of the time scale are estimated from 100 realizations of cusp widths obtained by fitting different harmonic amplitudes: sorting locations by cusp-integrated energy, we obtain the average harmonic amplitudes within each energy percentile. From these 100 averaged harmonic amplitudes, we obtain 100 values of λ^{-1}. If the fit to a percentile-averaged cusp does not converge to a reasonable value, for example when the harmonic amplitudes do not average to a cusp shape, that fit is discarded before estimating the mean time scale and its standard deviation.

4 Results

4.1 Spectral Properties of Tidal Currents

The rotary power spectral density for velocity, S_{rot}, is shown in Figure 3, calculated at each location and averaged within latitudinal bands of fixed width ($3.2° \approx 356$ km). Both plots are on a linear frequency axis and logarithmic spectral power axis. Spectra are distinguished by latitude because the inertial frequency varies from approximately 1 cpd to 1.5 cpd over the 1500 km meridional span of the study domain. The numerical values on the vertical axis correspond only to the spectrum of data in the 32.0°N-35.2°N range (blue); for clear differentiation, each successive spectrum is scaled by a factor of ten from its lower neighbor. Away from tidal and near-inertial frequencies, surface currents in this region have a spectral slope of approximately -1, i.e. $S \propto \mathrm{frequency}^{-1}$, indicated by the black curve. This slope holds at frequencies less than about 9 cpd; above this value, the spectra behave like white noise with spectral power orders of magnitude lower than the processes of interest.

The principal tidal peaks, clustered around 1 cpd and 2 cpd and denoted by vertical dashed lines, are prominent in all latitude bands. High-frequency, low-amplitude overtides (frequency $>$ 2 cpd) are also detected in surface currents, up to 7 cpd (not shown). This suggests that the observation network has a noise floor low enough to allow for the detection of signals that are orders of magnitude lower in power than the processes of primary interest to this study.

The center of the broad but distinct peak of the near-inertial response increases in frequency with increasing latitude as expected (note that negative frequencies corre-

spond to clockwise polarization). Additionally, the near-inertial peak becomes narrower and its center more energetic with increasing latitude, as evidenced in the right panel of Figure 3. These spectra are directly comparable to the analysis of Kim et al. (2011), who examined HFR data in the same region when the observational network was less than three years old and who resolved the same features (wind-driven and tidal peaks, including overtides, and a spectral slope of -1) across different grid resolutions.

At all latitudes, the semidiurnal tidal band exhibits a prominent cusp. The diurnal constituents' peaks, however, rise above a smaller cusp than the semidiurnal peaks rise above: this is most evident in the highest latitude spectrum (44.8°N-48.0°N), where the broad peak of the near-inertial response has minimal overlap with the diurnal band, shown up close in Figure 3b. At the latitudes considered here, semidiurnal internal waves can internally propagate but diurnal ones cannot propagate. The difference in cusp prominence for the superinertial semidiurnal versus subinertial diurnal signals is consistent with the internal semidiurnal wave field being modulated by low-frequency changes in stratification that are not expected to modulate the diurnal tide.

4.2 Harmonic Decomposition of Tidal Currents

We use the low-resolution spectra to inform the least squares harmonic fit to frequencies at a higher resolution, with Δf at the scale of the fundamental frequency of the record. Figure 4 shows the domain-wide average of the harmonic amplitude, defined as the sum of the squares of the sine and cosine coefficients, at 6 frequency bands (low-frequency, O_1 lunar diurnal, S_1 solar diurnal, N_2 lunar semidiurnal, M_2 lunar semidiurnal, and S_2 solar semidiurnal). These amplitudes are normalized by the non-constant frequency step Δf in order to obtain units of spectral power that can be compared despite differing values of Δf. Harmonic amplitudes at near-inertial frequencies are not shown in this study. Low-frequency signals, in particular the annual cycle S_a, are energetic and prominent, and are predominantly meridional in direction (distinction not shown), possibly due to the seasonally reversing surface flow within 100 km of the coast in the CCS (Rudnick et al., 2017) and other low-frequency variability of this current, which is predominantly parallel to the coast and therefore predominantly meridional in direction. The meridional component v similarly dominates at most higher frequencies. The prominent peak at 1 cpd is non-tidal and possibly driven by diurnal winds, as the true S_1 tide is driven

primarily by diurnal atmospheric loading and is known to be much smaller than the primary gravitational tides (R. D. Ray & Egbert, 2004).

At semidiurnal frequencies, which are superinertial at these latitudes and therefore are expected to have a substantial baroclinic component, the subtraction of the FES2014 model typically reduces the total variance as observed by HFR. At M_2, the median fraction of remaining variance is 0.46, with 75.2% of locations exhibiting a decrease in variance. For S_2, the median is 0.54, with 76.2% of locations exhibiting a decrease. For N_2, these values are 0.52 and 70.2%. At diurnal frequencies, which are subinertial, subtraction of the FES2014 model does not typically reduce the total variance as observed by HFR. For O_1, the median fraction after model subtraction is 1.16, with 44.4% of locations reduced in variance, while for K_1 these values are 1.38 and 31.1%. The S_1 wind-driven current is much stronger than the modeled S_1 barotropic tide, and thus the median variance fraction after model subtraction is 0.99, with a narrow range of variability (90% of locations fall between 0.85 and 1.03). A value of 1 indicates no change in variance after model removal.

4.3 Phase Structure

Amplitude and phase can be calculated from harmonic coefficients and both are required to fully characterize some frequency component of a signal. The Greenwich phases of the M_2 harmonic of both u and v are shown in Figure 5. Panels (a,d) show the phase from harmonically decomposed HFR data, panels (b,e) show the phase of currents given by the FES2014 barotropic tide model, and panels (c,f) show the phase of the M_2 harmonic of HFR after removal of the barotropic model. The spatial structure of phase of the decomposed HFR data exhibits domain-wide ($\sim$1000 km-scale) coherence like the barotropic model, as well as smaller, 50 to 100 km-scale structures, which are not present in the model. The meridional current v is particularly coherent across the domain (Figure 5d), with an angular mean phase of 164° and 80% of grid points falling within ±45° of this mean. At all other frequencies in the M_2 band, including the frequencies corresponding to annual modulation, phases are distributed more uniformly on the interval [-180° 180°] (not shown) and therefore lack the partial domain-wide coherence observed at exactly the M_2 frequency.

After removal of the modeled barotropic component (Figure 5c,f), the apparent underlying domain-wide coherence largely disappears, leaving behind the smaller scale phase structure that is not visible in the barotropic tidal current and is suggestive of internal propagation. In the Southern California Bight, the phase generally varies across smaller distances than in the topographically simpler regions north of Point Conception (approximately 34.5°N).

4.4 Non-phase-locked Energy

Maps showing distribution of amplitude or a related quantity highlight regions of energetic tides, while maps of phase-locked energy indicate where the tidal peak is more or less prominent in relation to its cusp. Figure 6 shows the square root of the eddy kinetic energy of the M_2 tidal current (6a,c) and the fraction of energy that is considered phase-locked (6b,d). Panels 6a and 6b display these quantities from harmonically decomposed HFR data only, while panels 6c and 6d show these quantities after subtracting the barotropic model output. A general reduction in M_2 current energy is observed after barotropic removal, with a median variance reduction of 54%. The sites with the most energetic M_2 currents from HFR are at the mouth of the Columbia River, off Cape Mendocino, at the mouth of San Francisco Bay, and in the Southern California Bight, especially over the Santa Cruz Basin. These sites remain energetic after barotropic removal.

Histogram representations of the quantities in panels 6b and 6d are shown in Figure 7. The median fraction of phase-locked current variance from HFR alone is 53% with an interquartile range between 38% and 66%. After barotropic removal, the median is 33% with an interquartile range between 22% and 46%, indicating that the barotropic component represents a significant fraction of the phase-locked variance.

To evaluate the dominance of the barotropic component, we define the "total variance" as the sum of the variance of the modeled barotropic current and the variance of the difference between observations and the model:

$$F_{\mathrm{BT}} = \frac{\mathrm{var}(u_{\mathrm{FES}}) + \mathrm{var}(v_{\mathrm{FES}})}{\mathrm{var}(u_{\mathrm{FES}}) + \mathrm{var}(v_{\mathrm{FES}}) + \mathrm{var}(u_{\mathrm{HFR}} - u_{\mathrm{FES}}) + \mathrm{var}(v_{\mathrm{HFR}} - v_{\mathrm{FES}})}. \tag{4}$$

This is equivalent to one minus the baro*clinic* fraction of total variance.

Figure 8a shows the modeled barotropic variance as a fraction of this total variance. Values near 1 show that the barotropic component dominates near the Oregon Coast

and at locations where the observations are weakly energetic. Shaded regions indicate comparatively low-variability regions, where the denominator of equation (4) is below the 20th percentile (7.05×10^{-4} m^2s^{-2}). Figure 8b shows the fraction of phase-locked current variance within the $f_{M_2} \pm 5$ cpy band that is attributed to the barotropic model, which is considered to be completely phase-locked. The quantity in this panel equals that of Figure 6b minus that of Figure 6d. Alternatively, this can be viewed as the change in non-phase-locked variance fraction after subtracting the model. Regions with negative values have greater current variance after the removal of the barotropic component. A median of 17% of variance is attributed to the model, and in the 10% of locations that are best explained by the model, an average of $\geq$45% of the variance can be attributed to the model. Overall, the barotropic tide model has skill in explaining the phase-locked tide, as indicated by the preponderance of red regions in Figure 8b. Because observed and modeled currents are vector quantities, however, their subtraction does not uniformly reduce the tidal amplitude. For example, regions with low observed tidal variability may have opposite-pointing barotropic and baroclinic contributions that sum to a low-amplitude signal, with an increase in non-phase-locked energy fraction after vector subtraction of the barotropic component. A *decrease* in non-phase-locked variance fraction occurs at 25% of locations, predominantly where the angle between the observations and model is greater than 45° and thus where subtraction of the barotropic model does not substantially reduce the magnitude of the residual (not shown). These regions of non-phase-locked fraction decrease are also disproportionately where the observed phase-locked M_2 variance (i.e. peak only) is less than 3.63×10^{-4} m^2s^{-2}, the 25th percentile of that quantity (not shown).

The spatial autocorrelation of the phase-locked variance fraction (Figure 9) shows that spatial consistency of the skill of the barotropic tide varies by tidal constituent. Here, the correlation is averaged in 5 km-wide concentric bands except for the second bin, which is 10 km wide in order to obtain sufficient realizations. Spatial lags extend to a maximum of 150 km separation between observation locations. The distance at which correlation of this quantity drops to 0.5 is 45 km for O_1, 101 km for S_1, and 29 km for S_2, based on a linear interpolation of the discrete correlation. For M_2, this decorrelation distance drops from 24 km for the full signal to 15 km after the barotropic tide has been removed (red dash-dotted line). Error estimates are not shown because estimates converge after averaging thousands of realizations, from 7270 to 1.77×10^5 depending on the

bin. Correlation does not meaningfully differ when averaged over 10 km-wide bins: when interpolated to 1 km intervals, the difference in correlation between the two bin choices has a mean of zero and a standard deviation less than 0.007 for each tidal constituent. The diurnal O_1 and semidiurnal M_2 and S_2 tidal constituents all exhibit autocorrelations that decrease to zero at distances less than 150 km, while the wind-driven S_1 only drops to 0.5 at this distance, indicating that both propagating (superinertial, here semidiurnal) and non-propagating (subinertial, here diurnal) tides in this region have smaller spatial scales of non-phase-locked variability than diurnal S_1 surface currents. The autocorrelation of non-phase-locked variance fraction is reduced for M_2 at every non-zero lag after barotropic model removal; this may be due to the larger scales at which the barotropic phase varies (see Figure 5), the removal of which may intensify the effect of the barotropic residual's smaller scale.

4.5 Tidal Envelopes

Because the non-phase-locked tide results from tidal modulation, we first examine the amplitude modulation of the M_2 and S_2 tides as a function of time, considering the evolution of the semi-major axis length. The right panels of Figure 10 show the tidal envelopes at five specific locations (identified as 1-5 in the map in the left panel). If the tidal envelopes were effectively random processes or if they were controlled by physical mechanisms that varied by frequency, then we would expect no correlation between the M_2 and S_2 envelopes. Instead, as the line plots on the right suggest, these amplitudes can be strongly correlated. The map in Figure 10 shows that throughout the domain, the correlation between the M_2 and S_2 semi-major axis envelopes is mostly positive: for a 90% significance level, 38.2% of locations have a significant positive correlation, 60.0% fall within the non-significance range, and 1.9% have a significant negative correlation (or 8.4% of all negative values). Striped areas indicate regions where the absolute value of the correlation coefficient (correlation at zero lag) is less than the 90% significance threshold (Press et al., 1988) given the estimated number of degrees of freedom at each location based on the characteristic timescale of the M_2 and S_2 envelopes (for estimating timescales, see Chapter 17, von Storch & Zwiers, 2003). The significance threshold is spatially inhomogeneous, with a mean of 0.267 and standard deviation of 0.048. Regions with energetic semidiurnal tides, as shown by Figure 6a, exhibit significant positive correlation between the M_2 and S_2 envelopes, including the Southern California Bite, San Francisco

Bay, Cape Mendocino, and the mouth of the Columbia River. Five locations from these regions with significant cross-correlation at zero lag are selected and labeled (1-5), with the time series of their M_2 and S_2 semi-major axis envelopes plotted in Figure 10. The envelopes at each location vary at different time scales. Location (1) near the mouth of the Columbia River is strongly annually modulated: both constituents' envelopes are consistently stronger in summer, with currents roughly three times greater in magnitude than in winter. Location (2) is near Cape Mendocino and the Mendocino Ridge, and the constituents at this location vary at long time scales, with greater magnitude in the first half of the record than in the second half, though the summer magnitude of S_2 in 2018-2020 increases while that of M_2 does not. Location (3) near the entrance to the San Francisco Bay has a less heavily modulated M_2 envelope, while the S_2 envelope is seemingly strongly semiannually modulated. This is caused by the linear addition of the K_2 tidal constituent ($f_{K_2} = f_{S_2} + f_{S_{sa}}$), which is prominent at this location, and does not appear to be due to amplitude modulation of the S_2 constituent: the amplitudes of the harmonic constituents in the semidiurnal band (not shown) are only energetic at f_{K_2} and not $f_{S_2} - f_{S_{sa}}$. Location (4) is between Santa Cruz Island and the mainland, and also exhibits a strong K_2 peak, as well as annual modulation of both constituents. Location (5) is farther offshore, south of Santa Cruz and Santa Rosa Islands, and has a less dominant K_2 relative to S_2. The correlation coefficient of 0.77 observed here is greater than those of 99% of locations evaluated. Location (5) is tidally energetic (for M_2, $\sqrt{(\sigma_u + \sigma_v)/2} = 0.05913$ m s^{-1}) with high coverage (94.1%). Overall, the variance of the K_2 constituent is distributed similarly to those of M_2 and S_2 (not shown).

4.6 Modulation Time Scale

In addition to the time domain analysis above, modulation can also be examined in the frequency domain to obtain the average time scale of both phase and amplitude modulation. The time scale λ^{-1} is given by fitting harmonic amplitudes to the Lorentzian function in equation (3). Locations were sorted into percentile bins by total energy of the tidal band of interest (including the central peak), averaged by percentile, and fitted at non-peak frequencies to obtain a range of estimates of λ^{-1}. Values for time scales are similar whether the non-linear parameter of the fit is λ or λ^{-1} (values shown here were calculated from the former). The mean time scales obtained by this method are $\lambda^{-1}_{O_1}$ = 218 days (standard deviation 37 days, 90% falling between 172 and 275 days), $\lambda^{-1}_{M_2}$

= 243 days (standard deviation 31 days, 90% between 195 and 288 days), and $\lambda_{S_2}^{-1}$ = 181 days (standard deviation 24 days, 90% between 153 and 218 days). Of the 100 percentile-sorted fits for each of the cusps, two for O_1 and one for M_2 were omitted from averaging due to lack of convergence to reasonable values. Least squares fits to the median harmonic amplitude are shown in red in Figure 4.

5 Discussion

In this study, we sought to partition the variability of tidally-driven surface currents between phase-locked and non-phase-locked components. Our analysis of HFR data in the CCS indicates an inhomogeneous distribution of both phase-locked and non-phase-locked variability of the two prominent semidiurnal constituents M_2 and S_2. Most of our analysis is focused on M_2 due to its prominence, while diurnal tides, which are non-propagating, are not investigated as extensively. The FES2014 barotropic tide model is used to remove the barotropic component of the M_2 tidal current, which accounts for a substantial share of the observed phase-locked variance. The model appears to reasonably remove the domain-wide coherent component of M_2 tidal currents, leaving behind a more uniform distribution of tidal phase values on the interval [-180° 180°]. This is suggestive of the surface expression of baroclinic tides, the wavelengths of which are much smaller than the domain. Before removal, a median of 53% (interquartile range between 38% and 66%) of M_2 current variance is phase-locked, compared to a median of 33% (interquartile range between 22% and 47%) after removal. Overall, 75% of grid locations show a decrease in M_2 phase-locked variance fraction after model subtraction, and the distance at which the phase-locked variance fraction is 50% correlated drops from 24 km to 15 km. Our analysis yields a *mean* of 48% *non*-phase-locked variance before removal and 64% after. These are both higher than the 44% near-global total non-phase-locked fraction calculated by Zaron (2017) from SSH, which was considered a lower bound due to the analysis of only mode-1 internal tides as estimated from wavenumber spectra. The results of that study are not directly comparable to ours, as the two use a different definition for non-phase-locked variance fraction. Further differences between our analysis and that of Zaron (2017) include the examination of surface currents as opposed to surface height, a domain that is limited to a single coastal region, and our distinction by constituent but not by internal wave mode. Additionally, the high spatiotemporal res-

olution of HFR data may limit the value of comparisons with analyses of global altimeter data without carefully accounting for these differences.

The analysis in this study provides a conservative estimate of the non-phase-locked fraction of tidal current variance, as our harmonic analysis is limited to the tidal forcing frequency ± 5 cpy (see Figure 4). This is a narrow band in the frequency domain relative to the width of the total semidiurnal cusp evident from power spectra in Figure 3. We chose this band because it allows for clear distinction between energy associated with separate tidal peaks while still fitting to near-tidal energy that corresponds to amplitude and phase modulations at time scales of a few months.

At both diurnal and semidiurnal frequencies, tidal peaks are well-defined and are at least one order of magnitude more energetic than at near-tidal frequencies. All tidal bands exhibit tidal cusps, though those of the low-amplitude O_1 and N_2 are less pronounced. These cusps are similar in form for all major tidal bands at this frequency resolution and narrow band-width. This contrasts with the difference in cusp size over a wider range of frequencies between diurnal and semidiurnal bands in the power spectra. Secondary peaks rise above the cusps at ±1 cpy around the central tidal peak. Some of these peaks are constituents of the astronomical forcing: the K_1 tide, for example, is a major tidal constituent with $f_{K_1} = f_{S_1} + f_{S_a}$. For M_2, there is a weak solar gravitational effect on the moon's orbit that results in seasonal perturbations impacting M_2, but these perturbations are very small: processes driven by solar radiation with a strong seasonal cycle, including stratification, wind, and sea ice coverage, however, are much more important to the modulation of M_2 (Müller et al., 2014).

Regions with energetic M_2 tidal signals, including known internal tide generation sites like the Mendocino Escarpment (Althaus et al., 2003) and Santa Cruz Basin (Buijsman et al., 2012), exhibit more strongly phase-locked signals. This is expected for locally generated internal tides, as such waves have not propagated far from their generation sites and become more incoherent through interaction with varying stratification and currents. Remotely generated internal tides propagating from outside the observed region are expected to lose coherence with forcing between their generation and observation sites and thus have a similar phase-locked energy fraction throughout the study region. The slowly evolving envelopes of the M_2 and S_2 current semi-major axes exhibit significant correlation coefficients (cross-correlation at zero lag) at several locations in

the domain, including near local generation sites (Figure 10). The envelopes are assumed to contain information about external modulation, as the lunar and solar forcing mechanisms that drive these constituents are independent and highly stable in time and therefore should not impart modulation, except for long-period modulation like that of the 18.6-year lunar nodal cycle (Doodson & Lamb, 1924; Cherniawsky et al., 2010). The fact that high cross-correlation tends to be observed near generation sites, where modulation related to propagation through a varying medium is expected to be weakest, may be due to the higher signal-to-noise ratio near generation sites allowing even weak modulation to be detectable. Signals farther from generation sites may have dropped below minimum noise-levels required for recovering envelopes or they may require more frequencies to be fitted due to extensive modulation. Additionally, we hypothesize that stratification variability at the generation sites is responsible for the weaker but non-zero tidal modulation observed at these locations, and is the most easily-observed amplitude modulation that both tidal constituents exhibit.

The processes that modulate the M_2 and S_2 currents appear to vary throughout the study domain, suggesting local modulation is captured in Figure 10. The strongly annual modulation at the mouth of the Columbia River is likely due to the substantial seasonal change in stratification associated with the seasonally shifting Columbia River plume (B. M. Hickey et al., 1998; B. Hickey et al., 2005; Thomas & Weatherbee, 2006; Burla et al., 2010). The Columbia River plume is known to be tidally pulsing and to generate internal waves, a process separate from the topographical generation of internal tides (Nash & Moum, 2005) The summer magnitudes of both constituents at this location are roughly three times the magnitudes in winter. Near Cape Mendocino, the envelopes of M_2 and S_2 current ellipses are also highly correlated but at nonperiodic time scales much longer than the tidal period, which is also typical of most locations with correlated amplitudes. Annual modulation is also observed throughout the domain, as evidenced by peaks at $f_{M_2} \pm f_{S_a}$ and $f_{S_2} \pm f_{S_a}$ in Figure 4, suggesting that both seasonal and interannual processes modulate tidal currents and lead to the non-phase-locked tide. The correlation of the modulation of the independently-forced M_2 and S_2 currents indicates that both respond similarly to the same processes in the ocean.

Lorentzian fits to the cusps of O_1, M_2, and S_2 indicate phase and/or amplitude modulation of these constituents at time scales in the range of 180 to 240 days. Zaron (2022) performed a similar fit for the M_2 cusp and obtained latitude-band averaged values for

λ^{-1} ranging from 151 days to 234 days. Our analogous value of $\lambda_{M_2}^{-1} = 243$ days is larger than the largest value in that study, though our range of values overlaps that of Zaron (2022). Other differences between the fitting procedures may explain this discrepancy: we omit tidal peaks and fit coastal surface current data to a Lorentzian probability density function within a band of $f_{M_2} \pm 5$ cpy and $\Delta f = 1/9$ cpy, while Zaron (2022) uses FES2014 to remove barotropic tides (among other corrections) to fit global altimeter data to a Lorentzian cumulative density function within a band of $f_{M_2} \pm 12.8$ cpy and $\Delta f = 1/4$ cpy. The relative agreement of time scales given by similar analysis of different physical quantities suggests both are modulated by the same processes.

6 Conclusions

We use least squares harmonic analysis to characterize the tidal components of over 9 years of hourly coastal surface currents as observed by high-frequency radar. The HFR network provides data at a spatial resolution comparable to that of recent and upcoming Earth-observing satellite missions. The length and sampling rate of these records enable us to recover details about the modulation of tidal processes at time scales up to a few years. The removal of the more predictable barotropic tide using a high-resolution finite element model enables analysis of the baroclinic component, which is expected to be much more sensitive to interaction with ocean processes due to its slower propagation speed and dependence on stratification.

The phase structure of tides in the California Current indicates a complicated field of internally propagating waves originating from several generation sites, with an inhomogeneous distribution of tidal energy and non-phase-locked tides. Near these generation sites, tidal currents are more energetic and more phase-locked, though the modulations of the amplitudes of the two dominant semidiurnal tides (M_2 and S_2) are most significantly correlated in these regions. These constituents are independently forced, suggesting that their amplitudes are modulated by the same processes. Stratification likely drives this, with tidal currents in the vicinity of the seasonal Columbia River plume exhibiting strongly annual modulation, while elsewhere modulation varies at a wider range of frequencies. Fitting harmonic amplitudes (here a spectral quantity) to a Lorentzian distribution indicates that the time scales of amplitude and/or phase modulation are 243 days for M_2, 181 days for S_2, and 218 days for the non-propagating O_1; the range of the

first of these values overlaps with those of the M_2 analysis of Zaron (2022), who examined global satellite altimetry data.

The length scale at which the fraction of phase-locked M_2 and S_2 surface current variance varies is on the order of tens of kilometers, which is resolved by HFR and contemporary and future satellite missions. The removal of the barotropic component via the FES2014 model reduces the correlation length scale of this quantity in M_2 from 24 km to 15 km and eliminates the domain-wide consistency of that constituent's phase.

With the recent launch of SWOT, incoming data will provide a global view of tidal variability at scales presently available only near well-observed coastlines. This study provides the share of non-phase-locked tidal surface current variance as well as the temporal and spatial scales of this quantity, which could help inform interpretation and assimilation of SWOT data (e.g. Metref et al., 2020, whose methodology omits internal tides). Additionally, the specific distribution of tidal variability off the US West Coast can help inform regional studies within this domain, for example to target or avoid locations with strongly modulated tidal surface currents. Combining results with stratification records, the predictability of tidal amplitude modulation could be assessed in future work, with implications for future satellite missions and for developing a more comprehensive understanding of the transformation of barotropic tides ultimately to turbulence.

Appendix A

The appendix summarizes the methodology of Kachelein et al. (2022), which is used in this study. It also describes how the baroclinic tidal component is estimated from the HFR data and barotropic tide model output.

A1 Overview of Harmonic Decomposition of HFR Data

A time series $u(t)$ that is discretely and possibly unevenly sampled may be modeled as the sum of sinusoids at M prescribed frequencies $\mathbf{f}$:

$$\mathbf{u} = \mathbf{H}\mathbf{x}_u + \mathbf{r}_u, \tag{A.1}$$

where $\mathbf{u}$ is the N-long column vector representation of $u(t)$, $\mathbf{H}$ is the N-by-$2M$ regressor matrix of sines and cosines at each frequency in $\mathbf{f}$, $\mathbf{x}_u$ are coefficients to the sines and cosines, and $\mathbf{r}_u$ is the residual time series that represents the unmodeled component of the time series. We use f for ordinary frequency rather than angular frequency $\omega = 2\pi f$ throughout. This is not to be confused with the common use of f to refer to the Coriolis parameter, the frequency of inertial oscillations, which are fitted but not investigated in this study.

The ordinary least squares approach (e.g. Draper & Smith, 1998; Foreman & Henry, 1989; Wunsch, 1996; Menke, 2018) seeks to find the $\mathbf{x}_u$ that minimizes the sum of the squares of $\mathbf{r}_u$. With only this constraint, the solution is

$$\hat{\mathbf{x}}_u = (\mathbf{H}^{\mathrm{T}}\mathbf{H})^{-1}\mathbf{H}^{\mathrm{T}}\mathbf{u}, \tag{A.2}$$

where the hat indicates that this is an estimator for some unknown true quantity. Given prior knowledge of $\mathbf{u}$, additional terms can be included in this solution that account for properties of $\mathbf{u}$ that equation A.2 does not consider, including the covariance of $\mathbf{x}_u$ and $\mathbf{r}_u$. Assuming independent Gaussian statistics of $\mathbf{x}_u$ and $\mathbf{r}_u$ and working from Bayes' theorem (see Lee, 2012; Kachelein et al., 2022), $\mathbf{x}_u$ can be estimated by

$$\hat{\mathbf{x}}_u = (\mathbf{H}^{\mathrm{T}}\mathbf{R}_{uu}^{-1}\mathbf{H} + \mathbf{P}_{uu}^{-1})^{-1}\mathbf{H}^{\mathrm{T}}\mathbf{R}_{uu}^{-1}\mathbf{u}, \tag{A.3}$$

where $\mathbf{R}$ denotes the expected autocovariance matrix of the residual of the subscripted quantity, here $\mathbf{R}_{uu} = \langle \mathbf{r}_u \mathbf{r}_u^{\mathrm{T}} \rangle$ and $\mathbf{P}$ denotes the expected autocovariance matrix of the model parameters of the subscripted quantity, here $\mathbf{P}_{uu} = \langle \mathbf{x}_u \mathbf{x}_u^{\mathrm{T}} \rangle$. These are estimated from the power spectrum of the data, $S_{uu}(f)$. Because the coefficients $\mathbf{x}_u$ are the amplitudes of sines and cosines, they also represent an estimate of the spectral power of $\mathbf{u}$

and therefore their autocovariance matrix $\mathbf{P}_{uu}$ may be estimated from the power spectrum at frequencies in $\mathbf{f}$. Similarly, the residual autocovariance $\mathbf{R}_{uu}$ may be estimated from the non-tidal component of the power spectrum via its Fourier transform.

A2 Removal of Barotropic Estimate

The harmonically decomposed HFR data are given as sine and cosine amplitudes, while the FES2014 barotropic tide model output is given by amplitude A and Greenwich phase lag G, which is related to tidal phase by $\phi = (V_\circ + u) - G$ (Lyard, 2022, personal communication), where $(\mathrm{V}_\circ + u)$ is the equilibrium argument for some reference time (Parker, 2007), in our case 2012-01-01 00:00:00 UTC. Values for the equilibrium argument can be computed or referenced in tidal charts, e.g. Zetler (1982). The sine amplitude a and cosine amplitude b can be calculated from total amplitude and phase by:

$$a = -A\sin\phi, \qquad b = A\cos\phi \tag{A.4}$$

Calculating the difference between two vector quantities that are sinusoidal in time is simpler when written as separate sine and cosine amplitudes than when written as total amplitude times a phase-shifted cosine:

$$u_3(t) = u_1(t) - u_2(t) = a_3\sin(\omega t) + b_3\cos(\omega t) = A_3\cos(\omega t + \phi_3), \tag{A.5}$$

where $a_3 = a_1 - a_2$ and $b_3 = b_1 - b_2$.

Acknowledgments

FES2014 was produced by Noveltis, Legos and CLS and distributed by Aviso+, with support from Cnes (`https://www.aviso.altimetry.fr/`). Surface current data are from the HFR National Network established by IOOS and are a component of the Global High Frequency Radar Network (Terrill et al., 2006; Roarty et al., 2019); these data are available for download at `https://HFRNet-tds.ucsd.edu/thredds/catalog.html`. This work has been supported by a Future Investigators in NASA Earth and Space Science and Technology award (80NSSC19K1342). In addition, Luke Kachelein, Bruce Cornuelle, Sarah Gille, and Matthew Mazloff acknowledge support from the NASA Surface Water and Ocean Topography Science Team (awards NNX16AH67G and 80NSSC20K1136), Luke Kachelein and Sarah Gille acknowledge support from the NASA Ocean Vector Winds Science Team

(award 80NSSC19K0059), and Sarah Gille also acknowledges support from the NASA Ocean Surface Topography Science Team (award 80NSSC21K1822).

Open Research

During review, data and scripts are available at the following Google Drive link: `https://drive.google.com/drive/folders/1IfZsxMFFMCNABFza490HwnYzD1TayJ54?usp=sharing`. Please note that scripts have been tested for functionality but are not final for archival purposes, and are working versions. Data are final versions ready for archival. For publication, a static DOI will be assigned for data and scripts.

References

Althaus, A. M., Kunze, E., & Sanford, T. B. (2003). Internal tide radiation from Mendocino Escarpment. *Journal of Physical Oceanography*, *33*(7), 1510-1527. doi: 10.1175/1520-0485(2003)033⟨1510:ITRFME⟩2.0.CO;2

Baines, P. (1982). On internal tide generation models. *Deep Sea Research Part A. Oceanographic Research Papers*, *29*(3), 307-338. doi: 10.1016/0198-0149(82)90098-X

Barrick, D. E., & Lipa, B. J. (1997). Evolution of bearing determination in hf current mapping radars. *Oceanography*, *10*(2), 72–75. Retrieved from `http://www.jstor.org/stable/43924800`

Bishop, T. N., Bube, K. P., Cutler, R. T., Langan, R. T., Love, P. L., Resnick, J. R., ... Wyld, H. W. (1985). Tomographic determination of velocity and depth in laterally varying media. *Geophysics*, *50*(6), 903-923. doi: 10.1190/1.1441970

Buijsman, M. C., Uchiyama, Y., McWilliams, J. C., & Hill-Lindsay, C. R. (2012). Modeling semidiurnal internal tide variability in the southern california bight. *Journal of Physical Oceanography*, *42*(1), 62 - 77. doi: 10.1175/2011JPO4597.1

Burla, M., Baptista, A. M., Zhang, Y., & Frolov, S. (2010). Seasonal and interannual variability of the Columbia River plume: A perspective enabled by multiyear simulation databases. *Journal of Geophysical Research: Oceans*, *115*(C2). doi: 10.1029/2008JC004964

Centurioni, L. R., Ohlmann, J. C., & Niiler, P. P. (2008). Permanent meanders in the california current system. *Journal of Physical Oceanography*, *38*(8), 1690 - 1710. doi: 10.1175/2008JPO3746.1

Chavanne, C. P., & Klein, P. (2010). Can oceanic submesoscale processes be observed with satellite altimetry? *Geophysical Research Letters*, *37*(22). doi: 10.1029/2010GL045057

Cherniawsky, J. Y., Foreman, M. G. G., Kuh Kang, S., Scharroo, R., & Eert, A. J. (2010). 18.6-year lunar nodal tides from altimeter data. *Continental Shelf Research*, *30*(6), 575-587. (Tides in Marginal Seas - A special issue in memory of Prof Alexei Nekrasov) doi: 10.1016/j.csr.2009.10.002

Chiswell, S. M. (2002, 09). Energy Levels, Phase, and Amplitude Modulation of the Baroclinic Tide off Hawaii. *Journal of Physical Oceanography*, *32*(9), 2640-2651. doi: 10.1175/1520-0485(2002)032⟨2640:ELPAAM⟩2.0.CO;2

Codiga, D. L. (2011, 1). *Unified tidal analysis and prediction using the utide matlab functions* (Tech. Rep.). Graduate School of Oceanography, University of Rhode Island, Narragansett, RI. Retrieved from `ftp://www.po.gso.uri.edu/pub/downloads/codiga/pubs/2011Codiga-UTide-Report.pdf` (59pp.)

Colosi, J. A., & Munk, W. (2006). Tales of the Venerable Honolulu Tide Gauge. *Journal of Physical Oceanography*, *36*(6), 967 - 996. doi: 10.1175/JPO2876.1

Doodson, A. T., & Lamb, H. (1924). Perturbations of harmonic tidal constants. *Proceedings of the Royal Society of London. Series A, Containing Papers of a Mathematical and Physical Character*, *106*(739), 513-526. doi: 10.1098/rspa.1924.0085

Draper, N. R., & Smith, H. (1998). *Applied regression analysis* (3rd ed.). John Wiley & Sons, Ltd. doi: 10.1002/9781118625590

Dunphy, M., Ponte, A., Klein, P., & Le Gentil, S. (2017, 01). Low-mode internal tide propagation in a turbulent eddy field. *Journal of Physical Oceanography*, *47*. doi: 10.1175/JPO-D-16-0099.1

Dushaw, B. D., Howe, B. M., Cornuelle, B. D., Worcester, P. F., & Luther, D. S. (1995). Barotropic and baroclinic tides in the central North Pacific Ocean determined from long-range reciprocal acoustic transmissions. *Journal of Physical Oceanography*, *25*(4), 631 - 647. doi: 10.1175/1520-0485(1995)025⟨0631:BABTIT⟩2.0.CO;2

Egbert, G. D., & Erofeeva, S. Y. (2021). An approach to empirical mapping of incoherent internal tides with altimetry data. *Geophysical Research Letters*, *48*(24), e2021GL095863. doi: 10.1029/2021GL095863

Egbert, G. D., & Ray, R. D. (2000). Significant dissipation of tidal energy in the

deep ocean inferred from satellite altimeter data. *Nature*, *405*, 775-778. doi: 10.1038/35015531

Erofeeva, S. Y., Egbert, G. D., & Kosro, P. M. (2003). Tidal currents on the central Oregon shelf: Models, data, and assimilation. *Journal of Geophysical Research: Oceans*, *108*(C5). doi: 10.1029/2002JC001615

Foreman, M. G. G. (1977). Manual for tidal heights analysis and prediction. pacific marine science rep. 77-10 [Computer software manual]. Patricia Bay, BC, Canada.

Foreman, M. G. G., Cherniawsky, J. Y., & Ballantyne, V. A. (2009). Versatile harmonic tidal analysis: Improvements and applications. *Journal of Atmospheric and Oceanic Technology*, *26*(4), 806-817. doi: 10.1175/2008JTECHO615.1

Foreman, M. G. G., & Henry, R. F. (1989, September). The harmonic analysis of tidal model time series. *Advances in Water Resources*, *12*, 109-120. doi: 10.1016/0309-1708(89)90017-1

Fredj, E., Roarty, H., Kohut, J., Smith, M., & Glenn, S. (2016). Gap filling of the coastal ocean surface currents from hfr data: Application to the mid-atlantic bight hfr network. *Journal of Atmospheric and Oceanic Technology*, *33*(6), 1097-1111. doi: 10.1175/JTECH-D-15-0056.1

Garrett, C., & Kunze, E. (2007). Internal tide generation in the deep ocean. *Annual Review of Fluid Mechanics*, *39*(1), 57-87. doi: 10.1146/annurev.fluid.39.050905.110227

Gurgel, K.-W. (1994). Shipborne measurement of surface current fields by hf radar. In *Proceedings of oceans'94* (Vol. 3, p. III/23-III/27 vol.3). doi: 10.1109/OCEANS.1994.364167

Hickey, B., Geier, S., Kachel, N., & MacFadyen, A. (2005). A bi-directional river plume: The Columbia in summer. *Continental Shelf Research*, *25*(14), 1631-1656. doi: 10.1016/j.csr.2005.04.010

Hickey, B. M., Pietrafesa, L. J., Jay, D. A., & Boicourt, W. C. (1998). The Columbia River Plume Study: Subtidal variability in the velocity and salinity fields. *Journal of Geophysical Research: Oceans*, *103*(C5), 10339-10368. doi: 10.1029/97JC03290

Huang, X., Wang, Z., Zhang, Z., Yang, Y., Zhou, C., Yang, Q., ... Tian, J. (2018). Role of mesoscale eddies in modulating the semidiurnal internal tide: Observation

results in the northern South China Sea. *Journal of Physical Oceanography*, *48*(8), 1749-1770. doi: 10.1175/JPO-D-17-0209.1

Ide, K., Courtier, P., Ghil, M., & Lorenc, A. C. (1997). Unified notation for data assimilation: Operational, sequential and variational. *Journal of the Meteorological Society of Japan. Ser. II*, *75*(1B), 181-189. doi: 10.2151/jmsj1965.75.1B_181

Kachelein, L., Cornuelle, B. D., Gille, S. T., & Mazloff, M. R. (2022). Harmonic analysis of non-phase-locked tides with red noise using the red_tide package. *Journal of Atmospheric and Oceanic Technology*, *39*(7), 1031 - 1051. doi: 10.1175/JTECH-D-21-0034.1

Kim, S. Y., Cornuelle, B. D., & Terrill, E. J. (2010). Decomposing observations of high-frequency radar-derived surface currents by their forcing mechanisms: Decomposition techniques and spatial structures of decomposed surface currents. *Journal of Geophysical Research: Oceans*, *115*(C12). doi: 10.1029/2010JC006222

Kim, S. Y., & Kosro, P. M. (2013). Observations of near-inertial surface currents off oregon: Decorrelation time and length scales. *Journal of Geophysical Research: Oceans*, *118*(7), 3723-3736. doi: 10.1002/jgrc.20235

Kim, S. Y., Terrill, E. J., & Cornuelle, B. D. (2008). Mapping surface currents from HF radar radial velocity measurements using optimal interpolation. *Journal of Geophysical Research: Oceans*, *113*(C10). doi: 10.1029/2007JC004244

Kim, S. Y., Terrill, E. J., Cornuelle, B. D., Jones, B., Washburn, L., Moline, M. A., ... Kosro, P. M. (2011). Mapping the U.S. West Coast surface circulation: A multiyear analysis of high-frequency radar observations. *Journal of Geophysical Research: Oceans*, *116*(C3). doi: 10.1029/2010JC006669

Kosro, P. M. (2005). On the spatial structure of coastal circulation off newport, oregon, during spring and summer 2001 in a region of varying shelf width. *Journal of Geophysical Research: Oceans*, *110*(C10). doi: 10.1029/2004JC002769

Kurapov, A. L., Egbert, G. D., Allen, J. S., Miller, R. N., Erofeeva, S. Y., & Kosro, P. M. (2003). The M2 internal tide off Oregon: Inferences from data assimilation. *Journal of Physical Oceanography*, *33*(8), 1733 - 1757. doi: 10.1175/1520-0485(2003)033⟨1733:TMITOO⟩2.0.CO;2

Lee, P. M. (2012). *Bayesian statistics: An introduction* (4th ed.). Wiley. (ISBN: 978-1-1183-3257-3)

Leffler, K. E., & Jay, D. A. (2009). Enhancing tidal harmonic analysis: Robust (hy-

brid l1/l2) solutions. *Continental Shelf Research*, *29*(1), 78 - 88. (Physics of Estuaries and Coastal Seas: Papers from the PECS 2006 Conference) doi: 10.1016/j.csr.2008.04.011

Lipa, B., & Barrick, D. (1983). Least-squares methods for the extraction of surface currents from codar crossed-loop data: Application at arsloe. *IEEE Journal of Oceanic Engineering*, *8*(4), 226-253. doi: 10.1109/JOE.1983.1145578

Lyard, F. H., Allain, D. J., Cancet, M., Carrère, L., & Picot, N. (2021). FES2014 global ocean tide atlas: design and performance. *Ocean Science*, *17*(3), 615–649. doi: 10.5194/os-17-615-2021

Matte, P., Jay, D. A., & Zaron, E. D. (2013). Adaptation of classical tidal harmonic analysis to nonstationary tides, with application to river tides. *Journal of Atmospheric and Oceanic Technology*, *30*(3), 569-589. doi: 10.1175/JTECH-D-12-00016.1

Menke, W. (2018). *Geophysical data analysis : discrete inverse theory* (Fourth edition ed.). London, United Kingdom: Elsevier Ltd.

Metref, S., Cosme, E., Le Guillou, F., Le Sommer, J., Brankart, J.-M., & Verron, J. (2020). Wide-swath altimetric satellite data assimilation with correlated-error reduction. *Frontiers in Marine Science*, *6*. doi: 10.3389/fmars.2019.00822

Mitchum, G. T., & Chiswell, S. M. (2000). Coherence of internal tide modulations along the Hawaiian Ridge. *Journal of Geophysical Research: Oceans*, *105*(C12), 28653-28661. doi: 10.1029/2000JC900140

Morrow, R., Fu, L.-L., Ardhuin, F., Benkiran, M., Chapron, B., Cosme, E., ... Zaron, E. D. (2019). Global observations of fine-scale ocean surface topography with the Surface Water and Ocean Topography (SWOT) Mission. *Frontiers in Marine Science*, *6*. doi: 10.3389/fmars.2019.00232

Müller, M., Cherniawsky, J. Y., Foreman, M. G. G., & von Storch, J.-S. (2014, Feb 01). Seasonal variation of the M2 tide. *Ocean Dynamics*, *64*(2), 159-177. doi: 10.1007/s10236-013-0679-0

Munk, W. H., & Wunsch, C. (1998). Abyssal recipes II: Energetics of tidal and wind mixing. *Deep Sea Research Part I: Oceanographic Research Papers*, *45*(12), 1977-2010. doi: 10.1016/S0967-0637(98)00070-3

Munk, W. H., Zetler, B., & Groves, G. W. (1965). Tidal cusps. *Geophysical Journal of the Royal Astronomical Society*, *10*(2), 211-219. doi: 10.1111/j.1365-246X.1965

.tb03062.x

Nash, J. D., & Moum, J. N. (2005). River plumes as a source of large-amplitude internal waves in the coastal ocean. *Nature*, *437*(7057), 400–403. doi: 10.1038/nature03936

Nelson, A. D., Arbic, B. K., Zaron, E. D., Savage, A. C., Richman, J. G., Buijsman, M. C., & Shriver, J. F. (2019). Toward realistic nonstationarity of semidiurnal baroclinic tides in a hydrodynamic model. *Journal of Geophysical Research: Oceans*, *124*(9), 6632-6642. doi: 10.1029/2018JC014737

Parke, M. E., Stewart, R. H., Farless, D. L., & Cartwright, D. E. (1987). On the choice of orbits for an altimetric satellite to study ocean circulation and tides. *Journal of Geophysical Research: Oceans*, *92*(C11), 11693-11707. doi: 10.1029/JC092iC11p11693

Parker, B. B. (2007). *Tidal analysis and prediction.* NOAA NOS Center for Operational Oceanographic Products and Services, Silver Spring, MD. (NOAA Special Publication NOS CO-OPS 3) doi: http://dx.doi.org/10.25607/OBP-191

Pawlowicz, R., Beardsley, R., & Lentz, S. (2002). Classical tidal harmonic analysis including error estimates in MATLAB using T_TIDE. *Computers & Geosciences*, *28*(8), 929-937. doi: 10.1016/S0098-3004(02)00013-4

Ponte, A., & Klein, P. (2015, 02). Incoherent signature of internal tides on sea level in idealized numerical simulations. *Geophysical Research Letters*, *42*. doi: 10.1002/2014GL062583

Press, W. H., Flannery, B. P., Teukolsky, S. A., & Vetterling, W. T. (1988). *Numerical recipes in c.* New York: Cambridge University Press.

Radok, R., Munk, W., & Isaacs, J. (1967). A note on mid-ocean internal tides. *Deep Sea Research and Oceanographic Abstracts*, *14*(1), 121-124. doi: 10.1016/0011-7471(67)90035-6

Rainville, L., & Pinkel, R. (2006). Propagation of low-mode internal waves through the ocean. *Journal of Physical Oceanography*, *36*(6), 1220 - 1236. doi: 10.1175/JPO2889.1

Ray, R. (1993). Global ocean tide models on the eve of TOPEX/Poseidon. *IEEE Transactions on Geoscience and Remote Sensing*, *31*(2), 355-364. doi: 10.1109/36.214911

Ray, R. D., & Cartwright, D. E. (2001). Estimates of internal tide energy fluxes

from Topex/Poseidon Altimetry: Central North Pacific. *Geophysical Research Letters*, *28*(7), 1259-1262. doi: 10.1029/2000GL012447

Ray, R. D., & Egbert, G. D. (2004). The global s1 tide. *Journal of Physical Oceanography*, *34*(8), 1922 - 1935. doi: 10.1175/1520-0485(2004)034⟨1922:TGST⟩2.0.CO;2

Ray, R. D., & Mitchum, G. T. (1996). Surface manifestation of internal tides generated near Hawaii. *Geophysical Research Letters*, *23*(16), 2101-2104. doi: 10.1029/96GL02050

Ray, R. D., & Zaron, E. D. (2011). Non-stationary internal tides observed with satellite altimetry. *Geophysical Research Letters*, *38*(17). doi: 10.1029/2011GL048617

Roarty, H., Cook, T., Hazard, L., George, D., Harlan, J., Cosoli, S., ... Grilli, S. (2019). The global high frequency radar network. *Frontiers in Marine Science*, *6*, 164. doi: 10.3389/fmars.2019.00164

Rudnick, D. L., Zaba, K. D., Todd, R. E., & Davis, R. E. (2017). A climatology of the california current system from a network of underwater gliders. *Progress in Oceanography*, *154*, 64-106. Retrieved from `https://www.sciencedirect.com/science/article/pii/S0079661116302075` doi: https://doi.org/10.1016/j.pocean.2017.03.002

Savage, A. C., Arbic, B. K., Alford, M. H., Ansong, J. K., Farrar, J. T., Menemenlis, D., ... Zamudio, L. (2017). Spectral decomposition of internal gravity wave sea surface height in global models. *Journal of Geophysical Research: Oceans*, *122*(10), 7803-7821. doi: 10.1002/2017JC013009

Savage, A. C., Arbic, B. K., Richman, J. G., Shriver, J. F., Alford, M. H., Buijsman, M. C., ... Zamudio, L. (2017). Frequency content of sea surface height variability from internal gravity waves to mesoscale eddies. *Journal of Geophysical Research: Oceans*, *122*(3), 2519-2538. doi: 10.1002/2016JC012331

Savage, A. C., Waterhouse, A. F., & Kelly, S. M. (2020). Internal tide nonstationarity and wave–mesoscale interactions in the Tasman Sea. *Journal of Physical Oceanography*, *50*(10), 2931 - 2951. doi: 10.1175/JPO-D-19-0283.1

Schmidt, R. (1986). Multiple emitter location and signal parameter estimation. *IEEE Transactions on Antennas and Propagation*, *34*(3), 276-280. doi: 10.1109/TAP.1986.1143830

Shriver, J. F., Richman, J. G., & Arbic, B. K. (2014). How stationary are the internal tides in a high-resolution global ocean circulation model? *Journal of Geophysical Research: Oceans*, *119*(5), 2769-2787. doi: 10.1002/2013JC009423

Terrill, E., Otero, M., Hazard, L., Conlee, D., Harlan, J., Kohut, J., ... Lindquist, K. (2006). Data management and real-time distribution in the hf-radar national network. In *Oceans 2006* (p. 1-6). doi: 10.1109/OCEANS.2006.306883

Thomas, A. C., & Weatherbee, R. A. (2006). Satellite-measured temporal variability of the Columbia River plume. *Remote Sensing of Environment*, *100*(2), 167-178. doi: 10.1016/j.rse.2005.10.018

U.S. Integrated Ocean Observing System. (2016). Manual for real-time quality control of high frequency radar surface current data: a guide to quality control and quality assurance for high frequency radar surface current observations. version 1.0. [Computer software manual]. (58pp.) doi: 10.25607/OBP-1464

von Storch, H., & Zwiers, F. W. (2003). *Statistical analysis in climate research.* Cambridge University Press. (ISBN: 0-521-45071-3)

Wang, J., Fu, L.-L., Qiu, B., Menemenlis, D., Farrar, J. T., Chao, Y., ... Flexas, M. M. (2018). An observing system simulation experiment for the calibration and validation of the Surface Water Ocean Topography sea surface height measurement using in situ platforms. *Journal of Atmospheric and Oceanic Technology*, *35*(2), 281-297. doi: 10.1175/JTECH-D-17-0076.1

Wunsch, C. (1996). *The Ocean Circulation Inverse Problem.* Cambridge University Press. (ISBN: 0-521-48090-6)

Zaron, E. D. (2015). Nonstationary internal tides observed using dual-satellite altimetry. *Journal of Physical Oceanography*, *45*(9), 2239 - 2246. doi: 10.1175/JPO-D-15-0020.1

Zaron, E. D. (2017). Mapping the nonstationary internal tide with satellite altimetry. *Journal of Geophysical Research: Oceans*, *122*(1), 539-554. doi: 10.1002/2016JC012487

Zaron, E. D. (2022). Baroclinic tidal cusps from satellite altimetry. *Journal of Physical Oceanography*, *52*(12), 3123 - 3137. doi: 10.1175/JPO-D-21-0155.1

Zaron, E. D., & Ray, R. D. (2018). Aliased tidal variability in mesoscale sea level anomaly maps. *Journal of Atmospheric and Oceanic Technology*, *35*(12), 2421 - 2435. doi: 10.1175/JTECH-D-18-0089.1

Zetler, B. D. (1982). Computer applications to tides in the national ocean survey: Supplement to manual of harmonic analysis and prediction of tides (special publication no. 98) [Computer software manual]. La Jolla, California 92093.

Figures (temporary section)

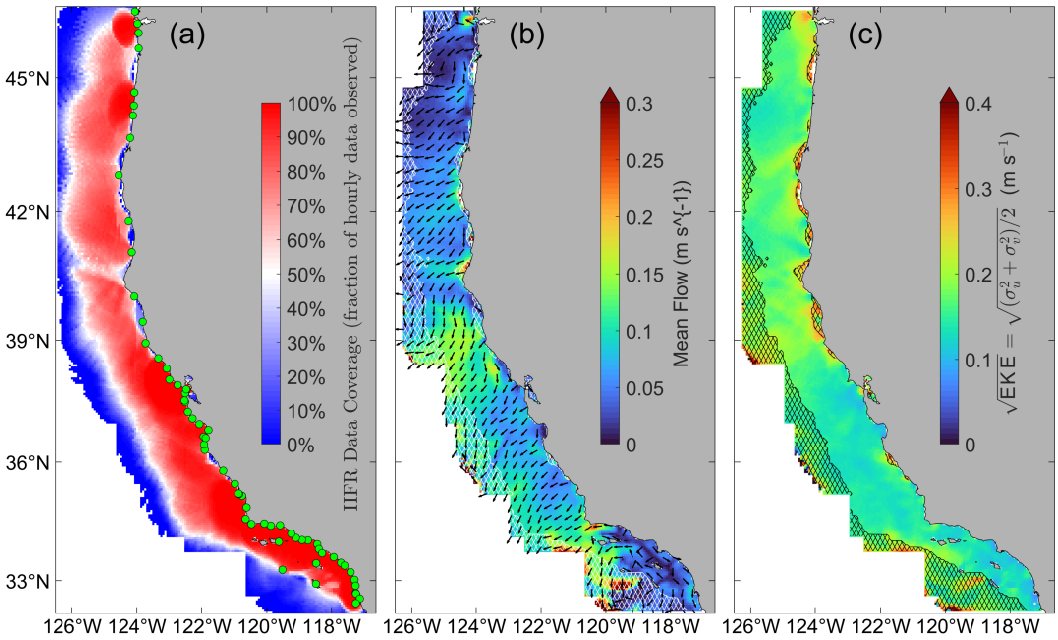

Figure 1: (a) High-frequency radar (HFR) network coverage in the study domain (percent hourly observations available). Green dots indicate locations of HFR stations. (b) Time-mean flow of the total current $\mathbf{u}$, including at locations not analyzed for tides. Colors indicate vector magnitude $|\mathbf{u}|$, uniform-length arrows indicate direction $\mathbf{u}/|\mathbf{u}|$. (c) Square root of the eddy kinetic energy of $\mathbf{u}$. Hatching in panels b and c indicates regions with less than 50% coverage, which were not analyzed for tides.

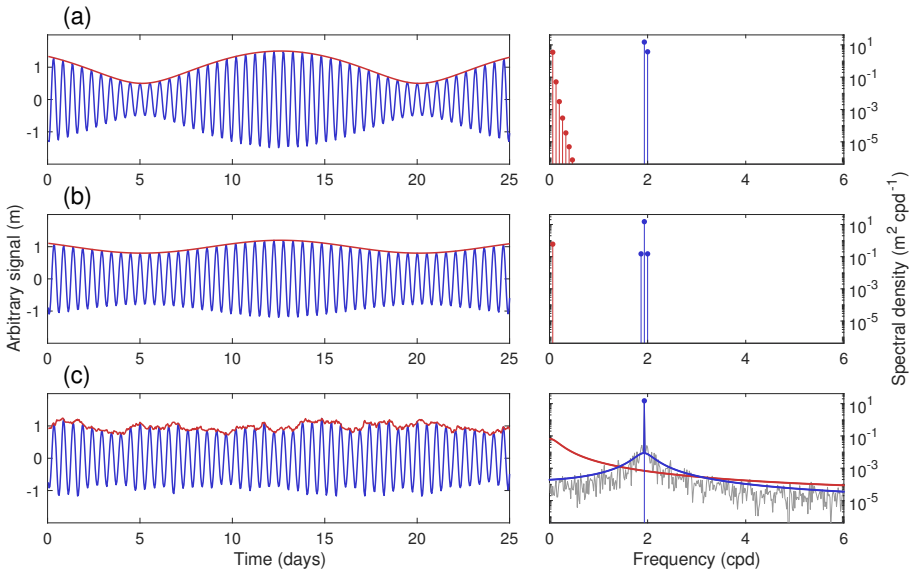

Figure 2: Constructed examples of (a) apparent modulation from linear addition of two tidal constituents and amplitude modulation by (b) sinusoidal and (c) broadband processes. The square of the Fourier transform of the broadband-modulated tidal signal is shown in gray in the bottom-right panel.

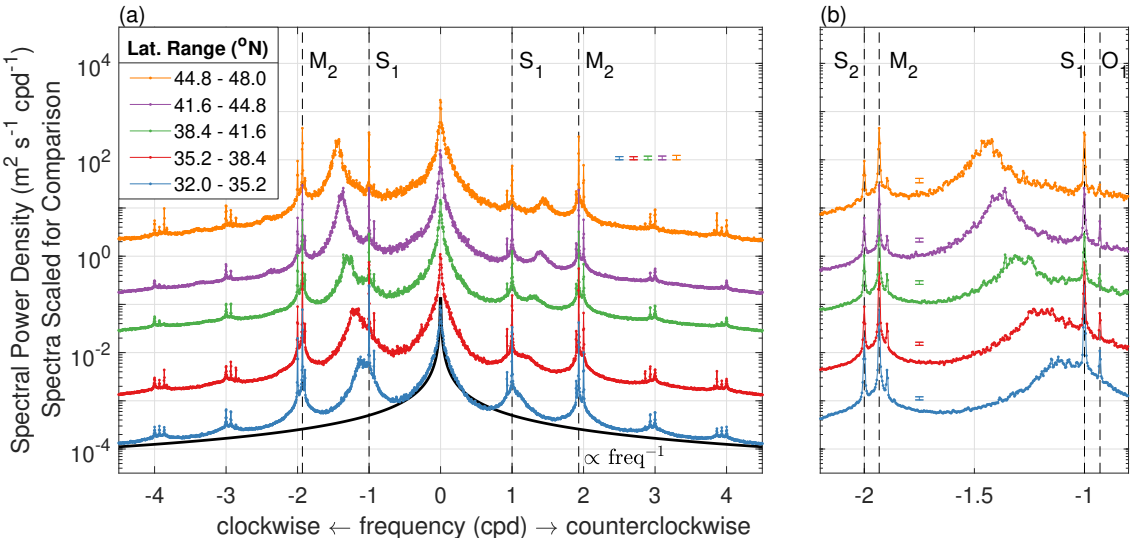

Figure 3: (a) Rotary power spectral density of surface current **u** from HFR averaged within five latitudinal bands, plotted on a linear frequency axis and logarithmic spectral power density axis. Spectra are vertically offset to avoid overlap. A black curve corresponding to a spectral slope of -1 is plotted for reference. Panel (b) displays the diurnal to semidiurnal band in the negative (clockwise) frequencies. Small colored vertical error bars indicate the 95% confidence ratio, which corresponds to a ratio valid at all magnitudes of the correspondingly colored spectral density.

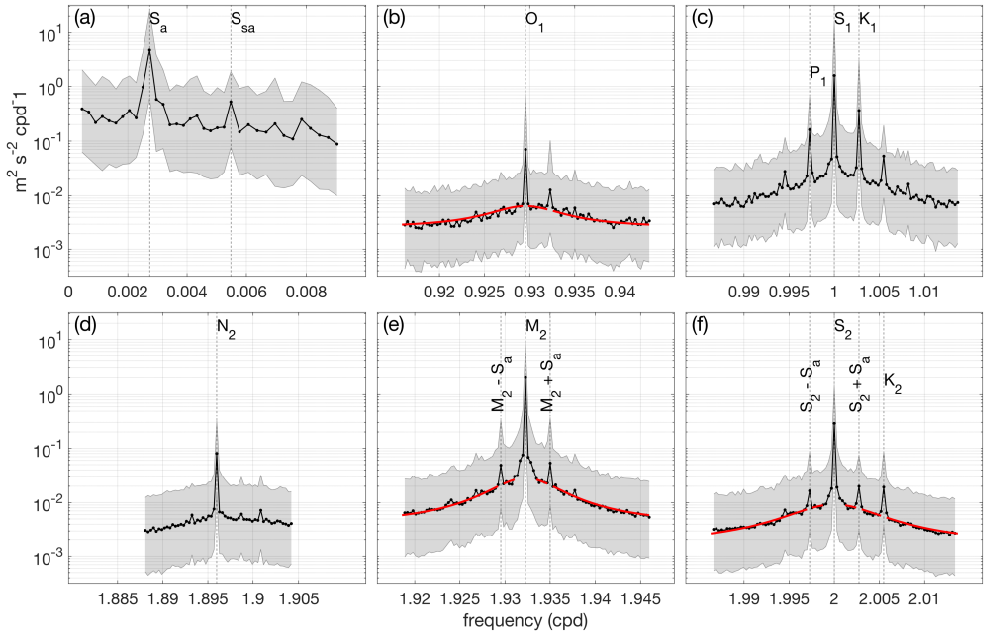

Figure 4: Domain-median total HFR current variance $\frac{1}{2}(\sigma_u^2 + \sigma_v^2)$ as given by harmonic decomposition, divided by (variable) frequency step $\Delta f(f)$ to give power spectral density. Shading indicates 5th and 95th percentiles. Prominent tidal constituents are labeled and all panels span the same vertical interval. Panel (a), which shows the variance recovered from harmonic decomposition at frequencies $\leq 1/110$ cpd, is scaled horizontally to accommodate fewer fitted frequencies, while panels (b-f) are all equally horizontally scaled. The red curves in panels (b), (e), and (f) are the non-linear least squares fitted curves to tidal cusps plotted at the fitted frequencies.

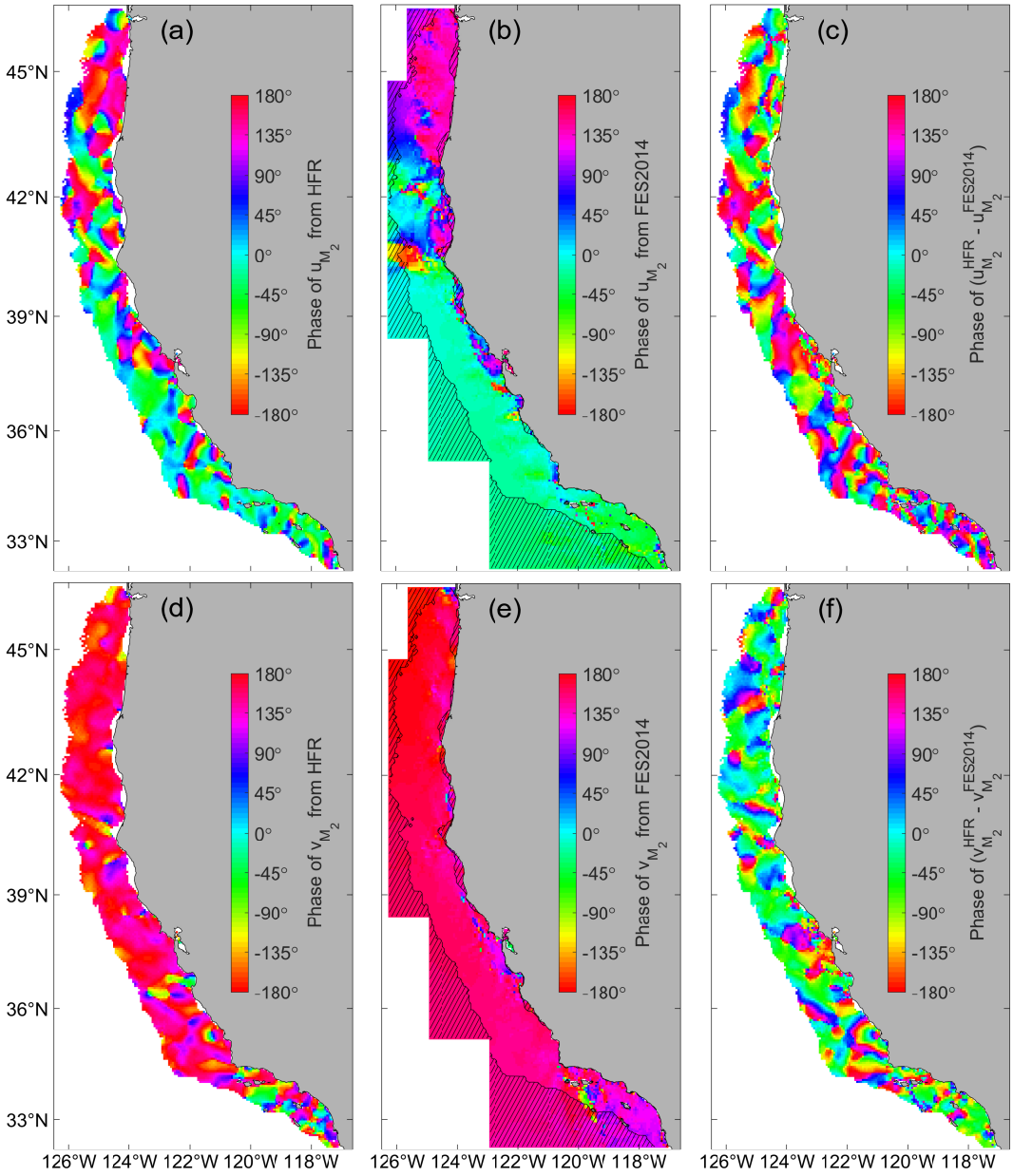

Figure 5: Tidal phase (degrees relative to Greenwich) of harmonically decomposed surface currents at the M_2 frequency. (a-c) show phase of the u-component, (d-f) show phase of the v-component. (a,d) show results from decomposed HFR data, (b,e) show results from the FES2014 tide model, and (c,f) show results from the difference between the data and model. Masking on panels (b,e) indicate locations where the model is defined but HFR data were not analyzed.

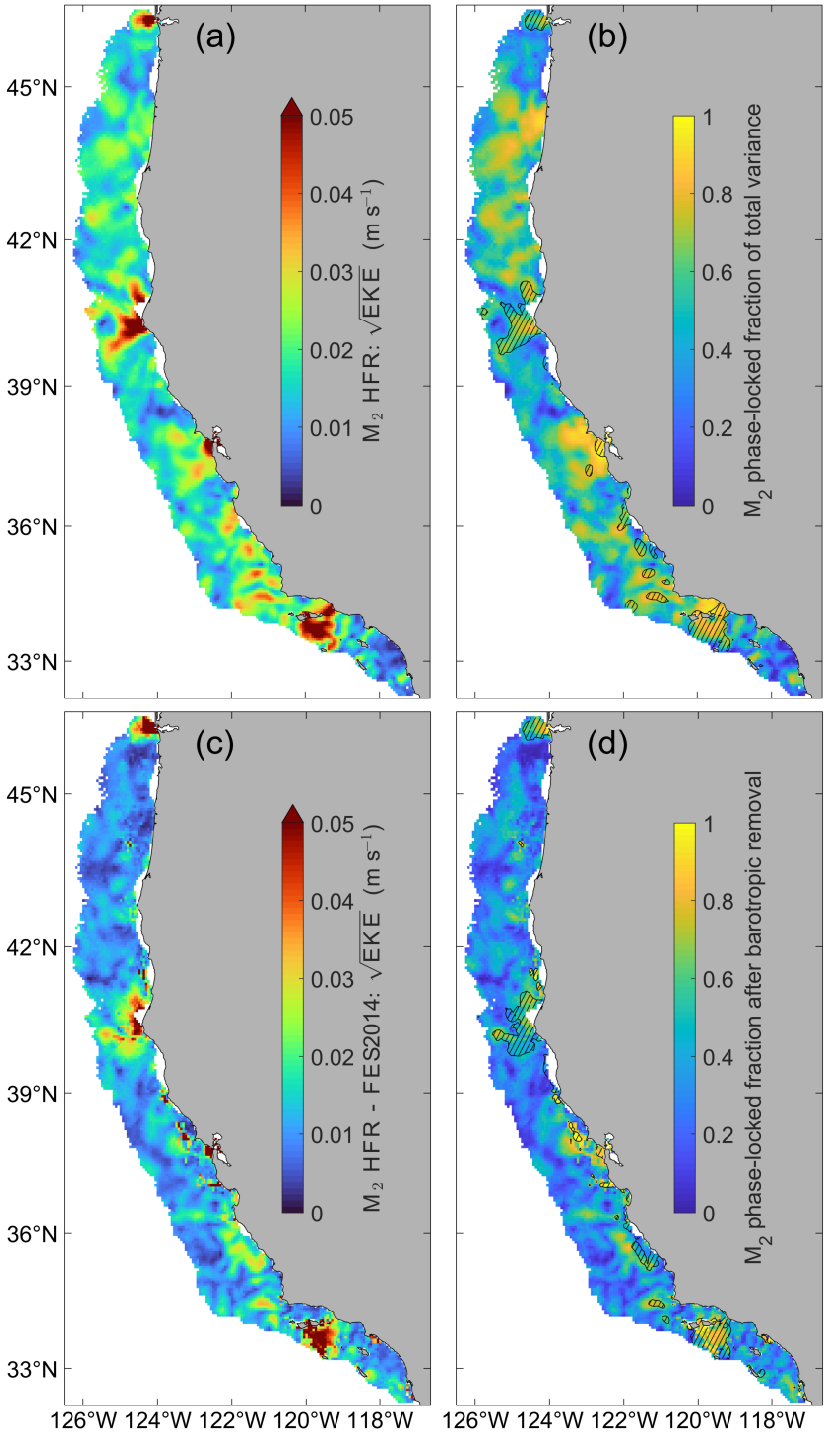

Figure 6: (a) Square root of eddy kinetic energy of the M_2 component of harmonically decomposed HFR data. (b) Fraction of M_2-band variance considered to be phase-locked without removal of the modeled barotropic component. (c-d) are analogous to (a-b) but with the modeled barotropic component removed. The "total variance" of the M_2 component is calculated within the frequency band $f_{M_2} \pm 5$ cpy. Striped regions in (b) indicate the top decile of variance, where the total variance within the M_2 band is $\geq 2.8 \cdot 10^{-3}$ $m^2 s^{-2}$, while striped regions in (d) indicate the top decile after barotropic removal, where

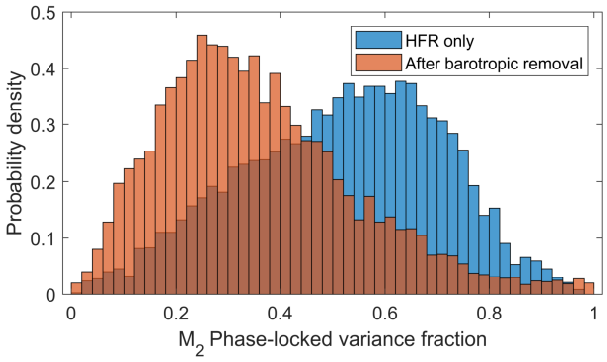

Figure 7: Histogram representation of the quantities in Figure 6 (B) and (D).

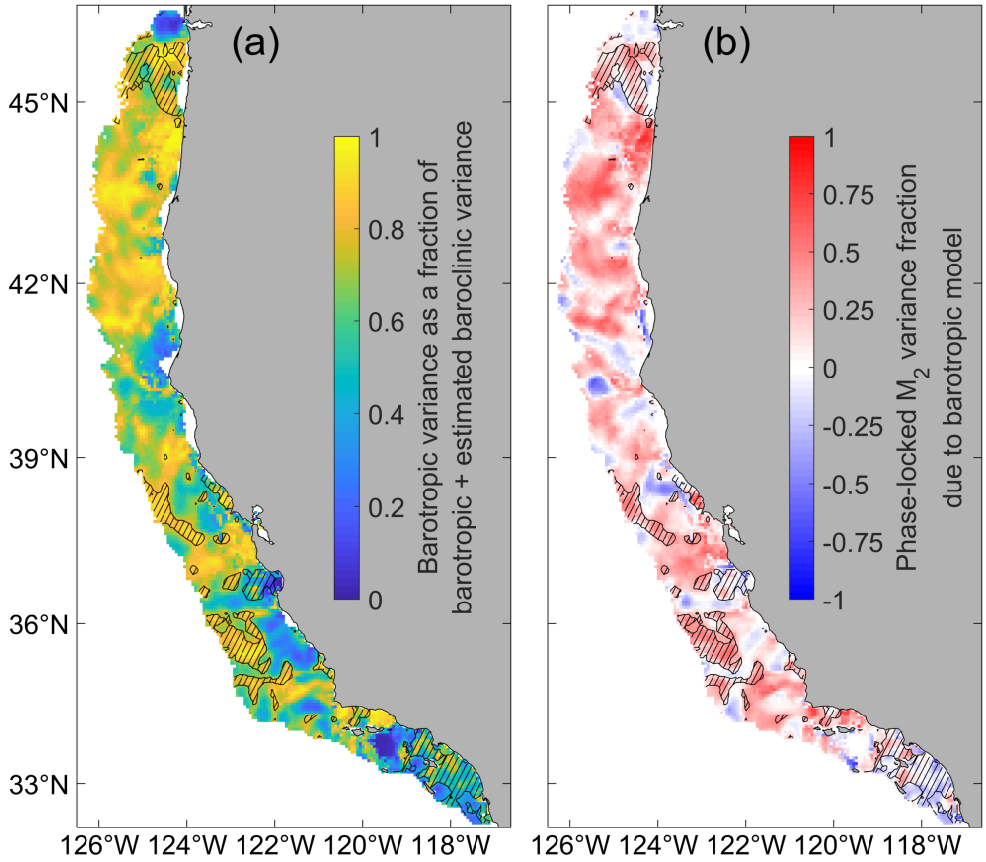

Figure 8: (a) Modeled barotropic M_2 variance as a fraction of total variance (modeled barotropic plus estimated baroclinic) and (b) the fraction of phase-locked M_2 variance attributable to the barotropic modeled component (the difference of Figure 6B and 6D). Negative values in panel (b) indicate greater current variance after the removal of the barotropic component. Regions with the 20% lowest total variance (the denominator in panel a) are hatched, i.e. where modeled barotropic variance plus estimated baroclinic variance is $\leq 7.05\times10^{-4}$ m^2s^{-2}.

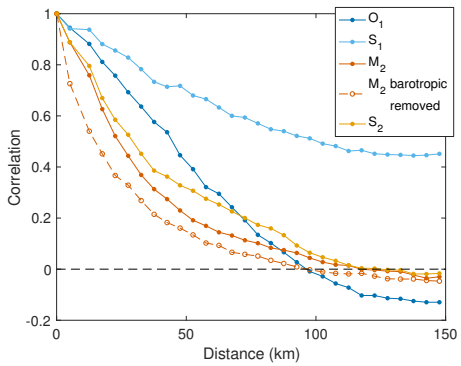

Figure 9: Isotropic correlation of phase-locked fraction of variance as a function of distance. Correlation drops to 0.5 at 45 km for O_1, 101 km for S_1, 24 km for M_2 (15 km for M_2 after barotropic removal), and 29 km for S_2. Error estimates are not shown due to strong convergence across $\mathcal{O}(10^3)$-$\mathcal{O}(10^5)$ realizations.

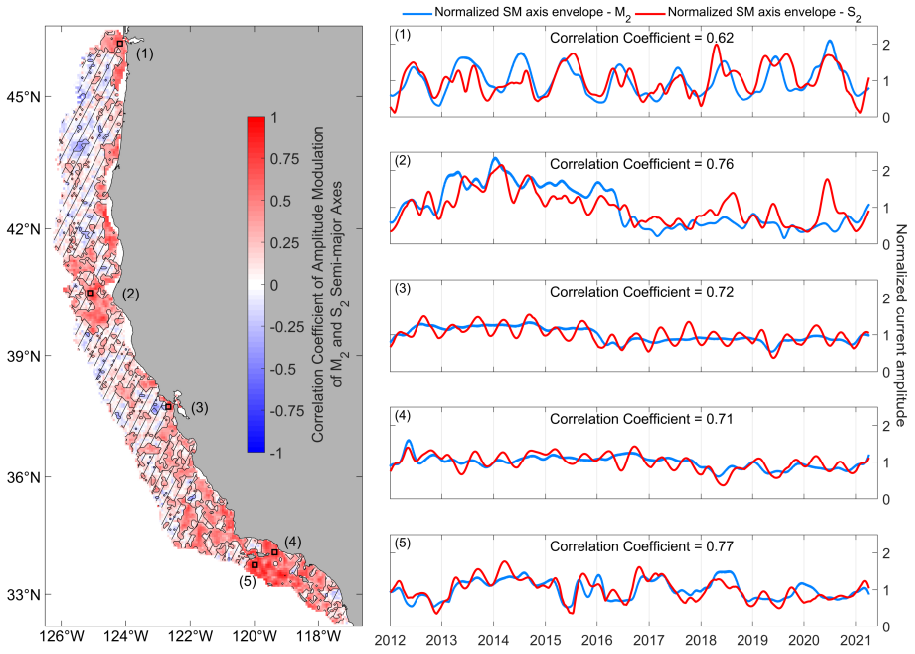

Figure 10: The correlation coefficients of the recovered modulation of the M_2 and S_2 vector current semi-major axes, calculated from the upper envelopes of $\sqrt{u_{M_2}^2 + v_{M_2}^2}$ and $\sqrt{u_{S_2}^2 + v_{S_2}^2}$. The modulating envelopes (alternatively the time-evolution of the semi-major axes) contain variance at fitted frequencies ≤ 5 cpy (periods ≥ 73 days), with coefficients in the frequency domain multiplied by a Hanning window in order to reduce spectral leakage. Striped regions indicate that the absolute value of the correlation coefficient is less than the 90% significance level calculated from the estimated number of degrees of freedom from the characteristic timescale of the M_2 and S_2 envelopes at each location. (1-5) are the normalized modulating envelopes for the semi-major axes of $\vec{u}_{M_2}$ and $\vec{u}_{S_2}$ at each location labeled on the map.

Figure 1.

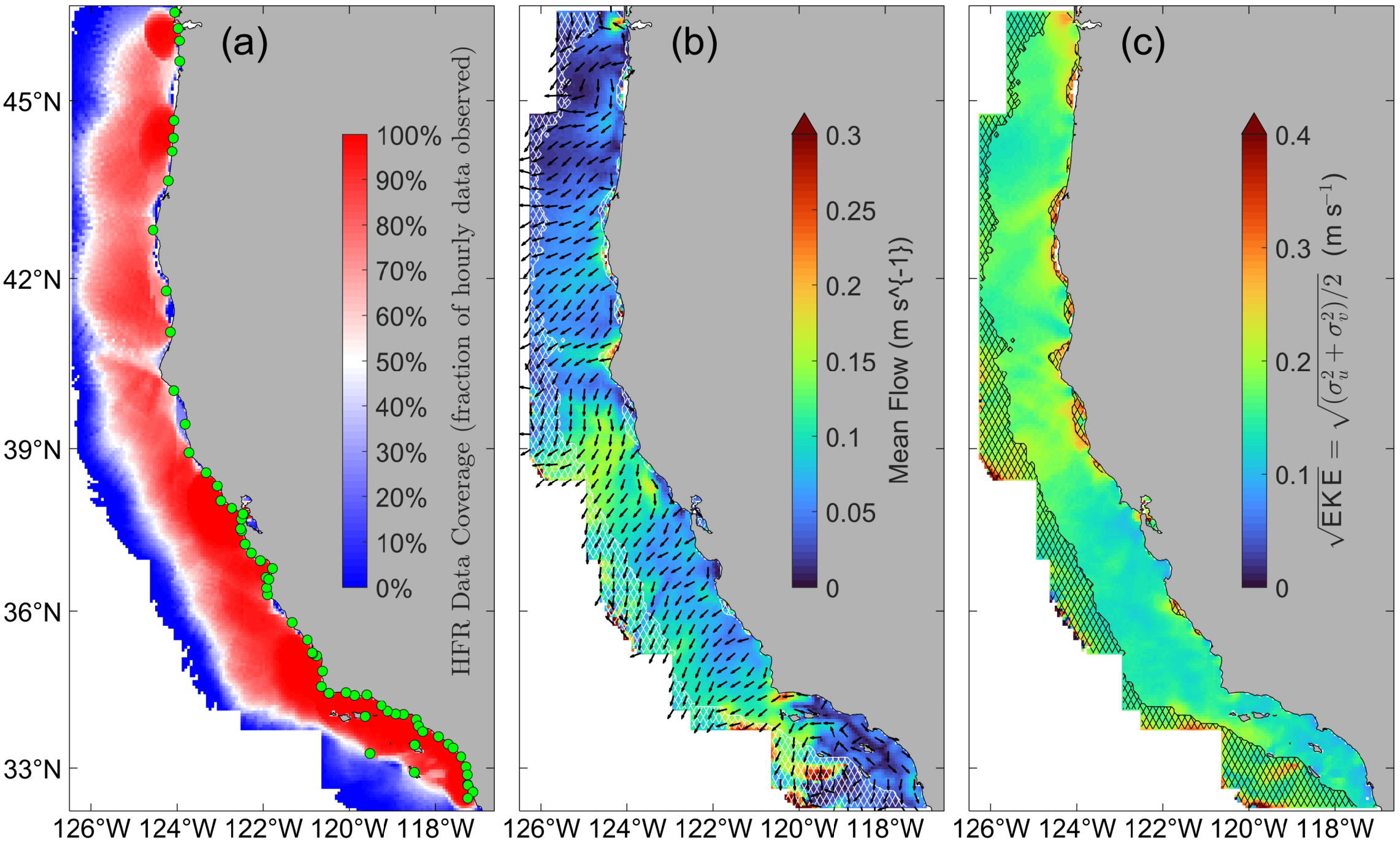
(a)
(b)
(c)
45°N
42°N
39°N
36°N
33°N
126°W 124°W 122°W 120°W 118°W
100%
90%
80%
70%
60%
50%
40%
30%
20%
10%
0%
HFR Data Coverage (fraction of hourly data observed)
0.3
0.25
0.2
0.15
0.1
0.05
0
Mean Flow (m s^{-1})
0.4
0.3
0.2
0.1
0
$\sqrt{\mathrm{EKE}} = \sqrt{(\sigma_u^2 + \sigma_v^2)/2}$ (m s^{-1})

Figure 2.

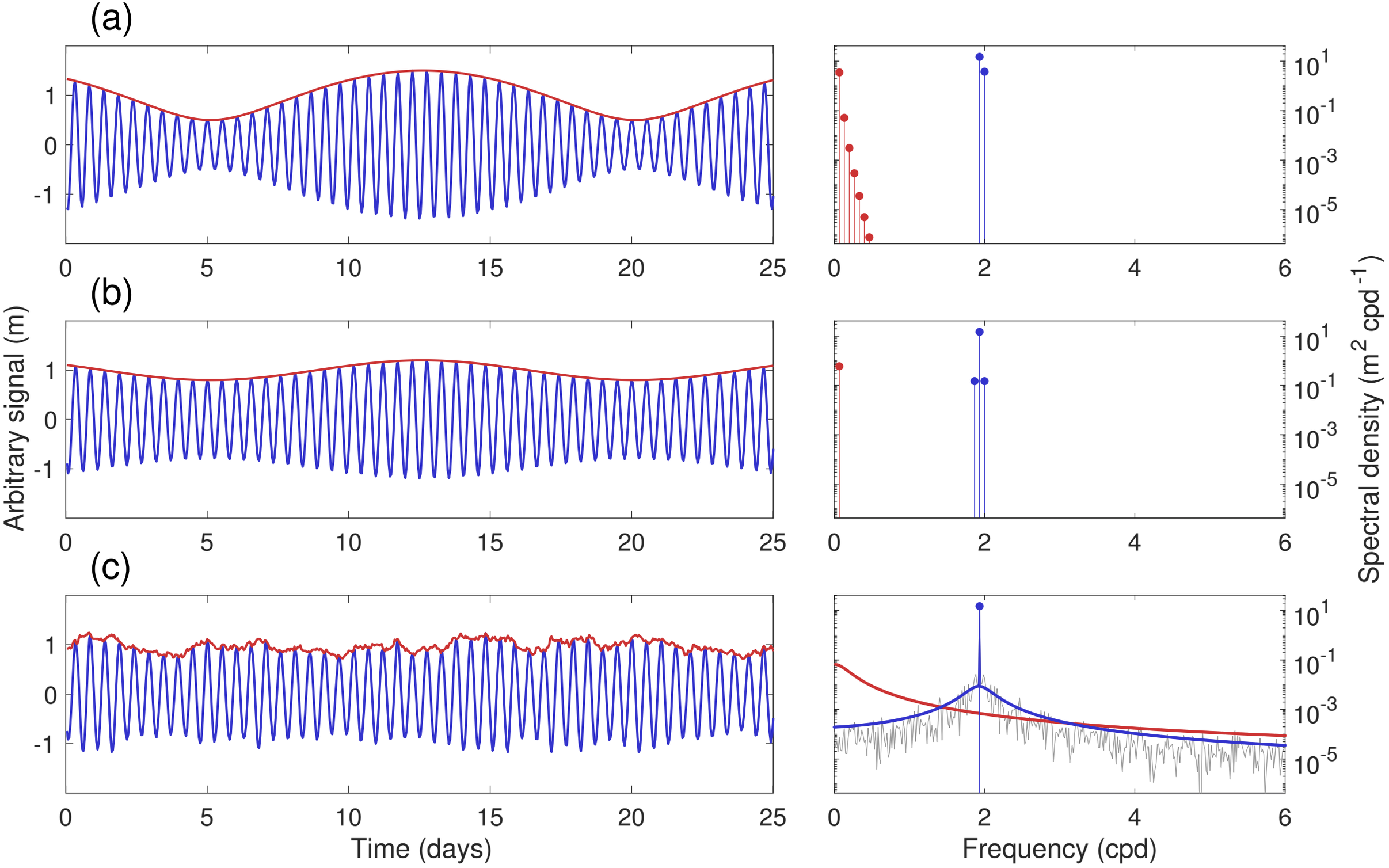
(a)
(b)
(c)
Arbitrary signal (m)
Time (days)
Frequency (cpd)
Spectral density (m^2 cpd^{-1})
1
0
-1
0
5
10
15
20
25
2
4
6
10^{1}
10^{-1}
10^{-3}
10^{-5}

Figure 3.

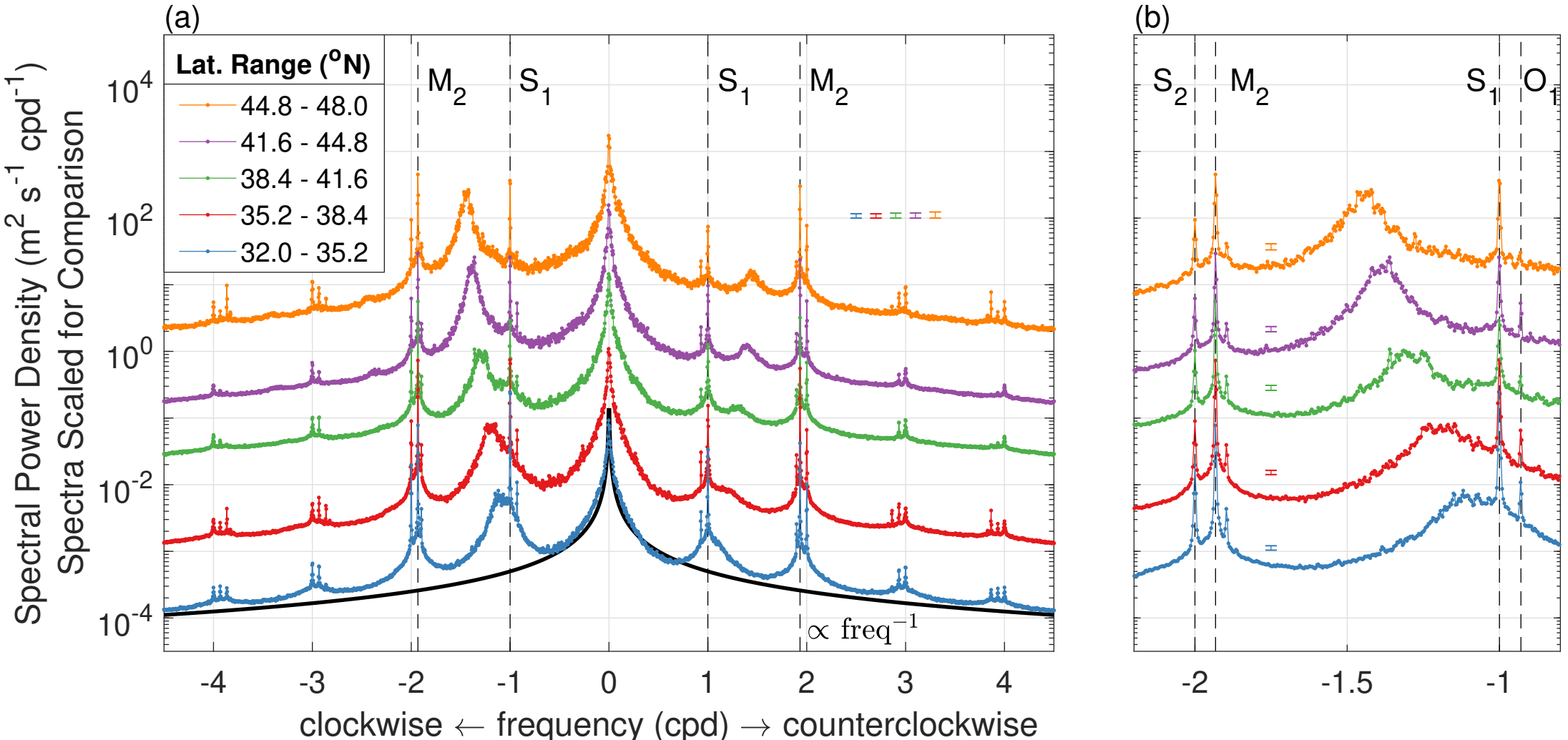
(a)
(b)
Lat. Range (°N)
44.8 - 48.0
41.6 - 44.8
38.4 - 41.6
35.2 - 38.4
32.0 - 35.2
M2
S1
S1
M2
S2
M2
S1
O1
∝ freq−1
Spectral Power Density (m2 s-1 cpd-1)
Spectra Scaled for Comparison
clockwise ← frequency (cpd) → counterclockwise

Figure 4.

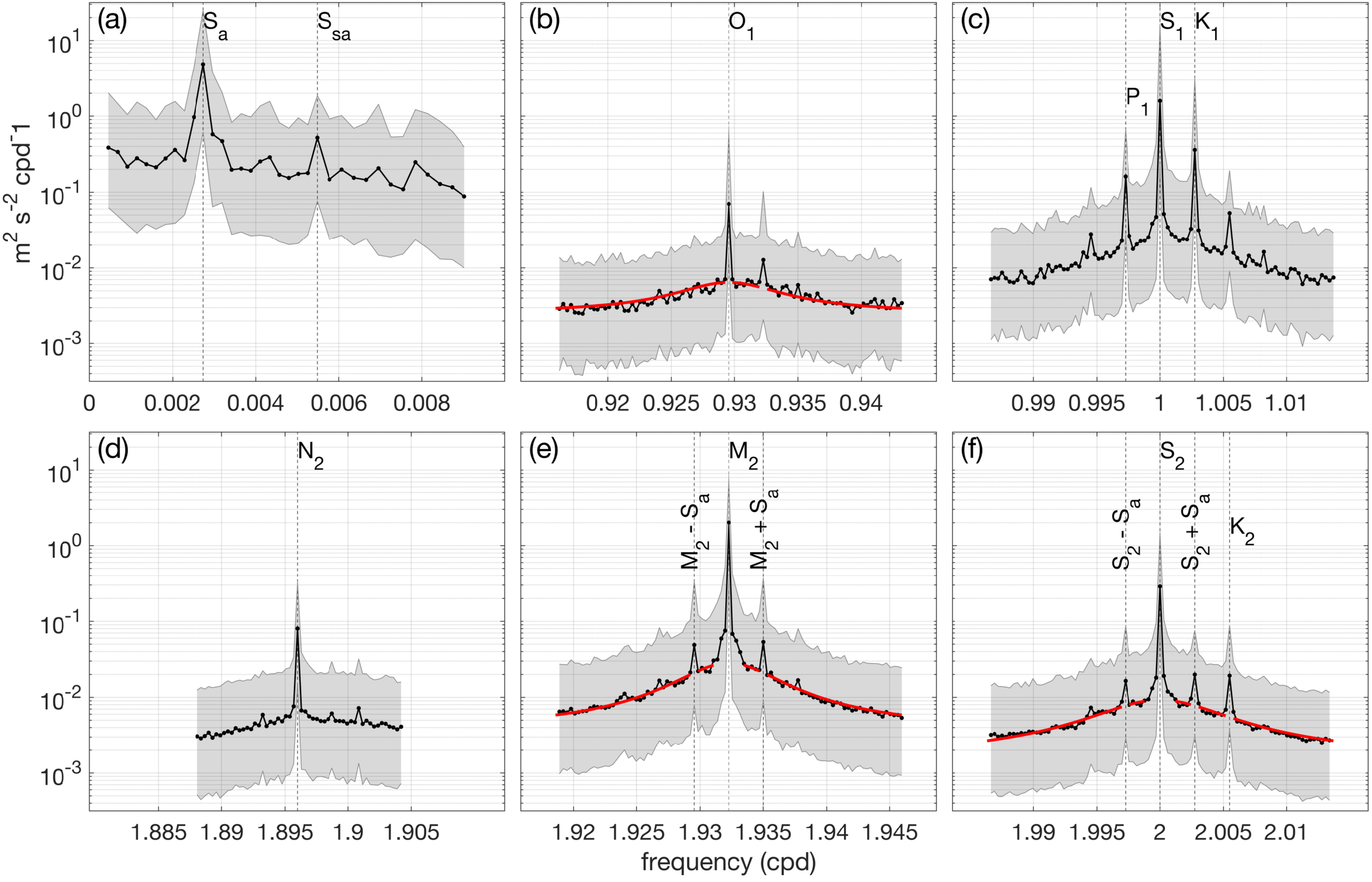
(a)
S_a
S_{sa}
(b)
O_1
(c)
S_1
K_1
P_1
(d)
N_2
(e)
M_2
$M_2 - S_a$
$M_2 + S_a$
(f)
S_2
$S_2 - S_a$
$S_2 + S_a$
K_2
$m^2\ s^{-2}\ cpd^{-1}$
frequency (cpd)

Figure 5.

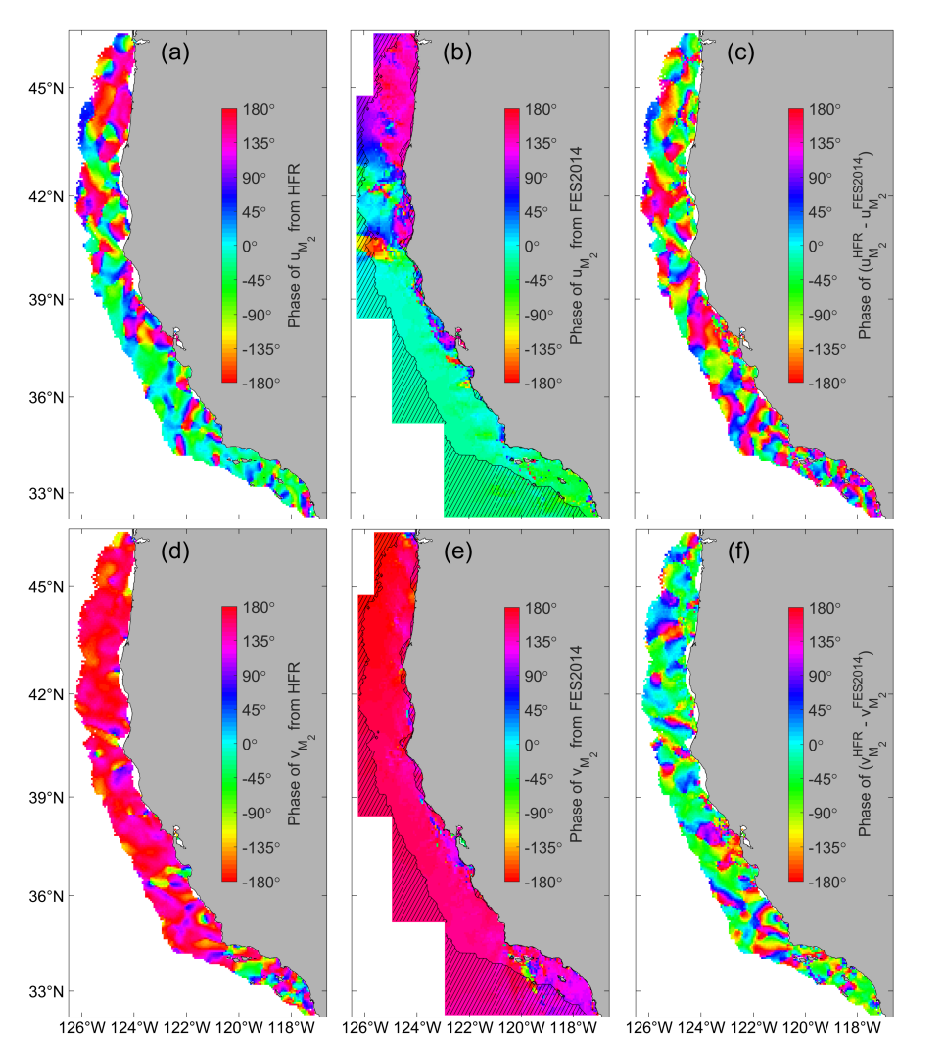
(a)
(b)
(c)
(d)
(e)
(f)
45°N
42°N
39°N
36°N
33°N
126°W 124°W 122°W 120°W 118°W
180°
135°
90°
45°
0°
-45°
-90°
-135°
-180°
Phase of u_{M_2} from HFR
Phase of u_{M_2} from FES2014
Phase of $(u_{M_2}^{HFR} - u_{M_2}^{FES2014})$
Phase of v_{M_2} from HFR
Phase of v_{M_2} from FES2014
Phase of $(v_{M_2}^{HFR} - v_{M_2}^{FES2014})$

Figure 6.

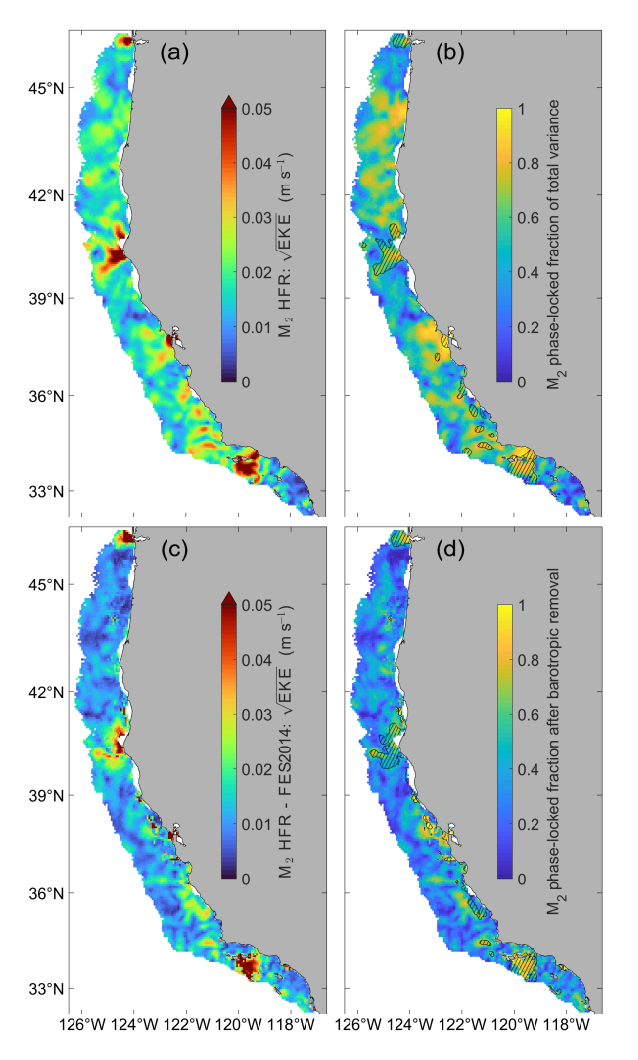
(a)
(b)
(c)
(d)
45°N
42°N
39°N
36°N
33°N
126°W 124°W 122°W 120°W 118°W
0.05
0.04
0.03
0.02
0.01
0
1
0.8
0.6
0.4
0.2
0
M2 HFR: √EKE (m s-1)
M2 phase-locked fraction of total variance
M2 HFR - FES2014: √EKE (m s-1)
M2 phase-locked fraction after barotropic removal

Figure 7.

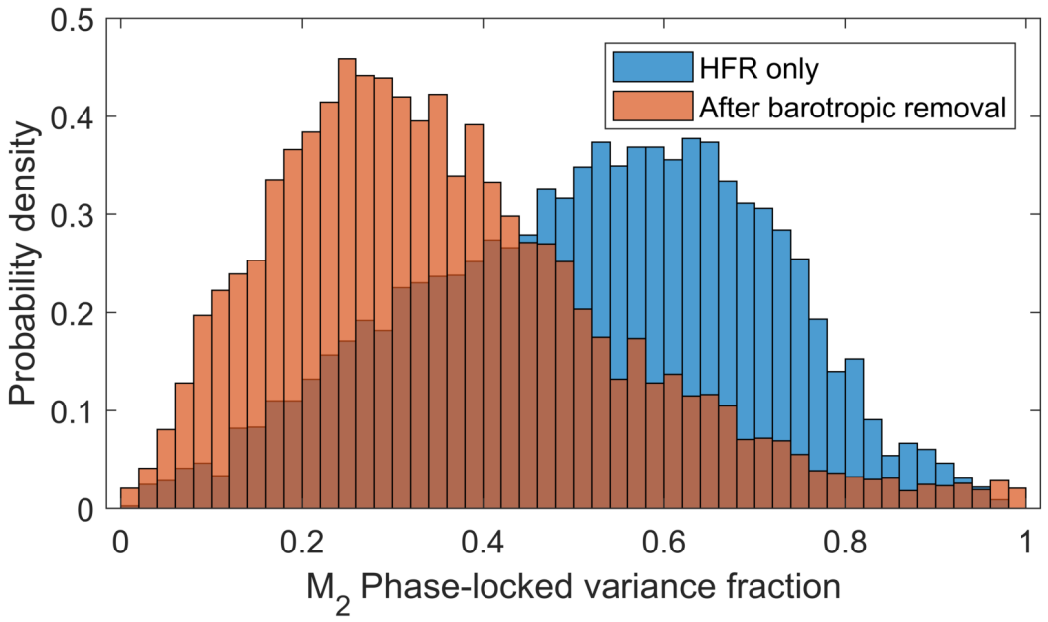
HFR only
After barotropic removal
Probability density
0.5
0.4
0.3
0.2
0.1
0
0
0.2
0.4
0.6
0.8
1
M2 Phase-locked variance fraction

Figure 8.

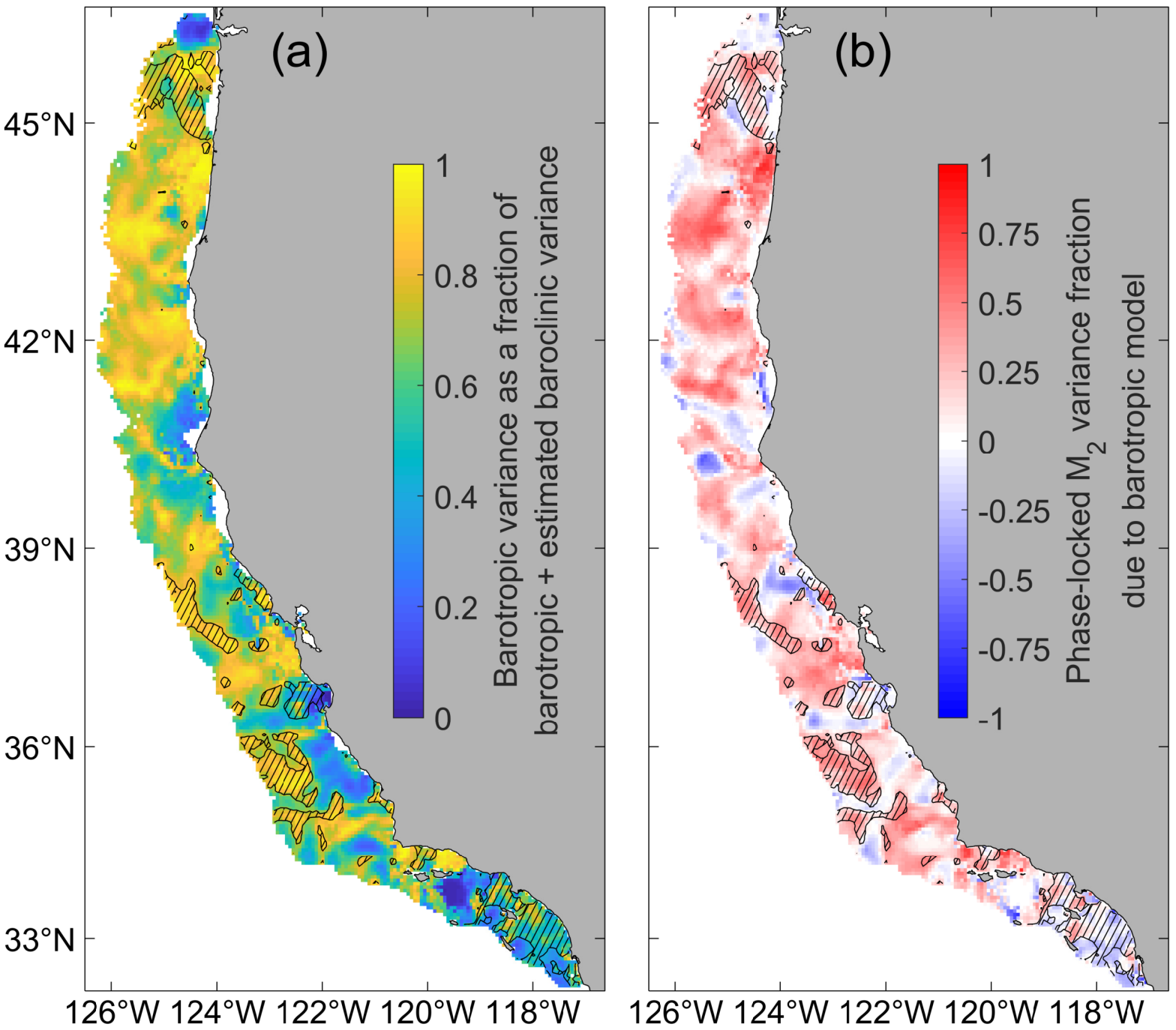
(a)
(b)
45°N
42°N
39°N
36°N
33°N
126°W 124°W 122°W 120°W 118°W
126°W 124°W 122°W 120°W 118°W
1
0.8
0.6
0.4
0.2
0
Barotropic variance as a fraction of barotropic + estimated baroclinic variance
1
0.75
0.5
0.25
0
-0.25
-0.5
-0.75
-1
Phase-locked M_2 variance fraction due to barotropic model

Figure 9.

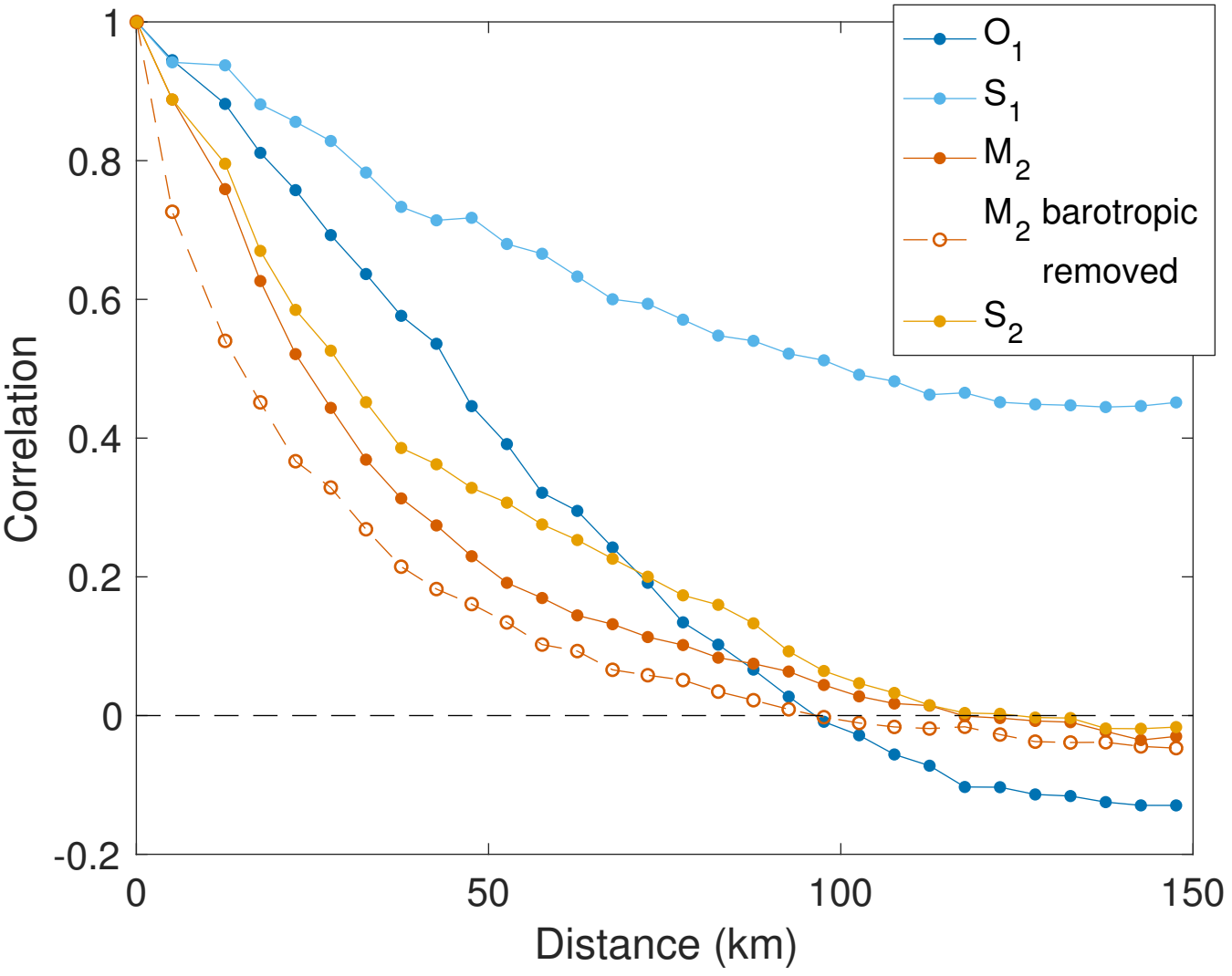
1
0.8
0.6
0.4
0.2
0
-0.2
Correlation
0
50
100
150
Distance (km)
O1
S1
M2
M2 barotropic removed
S2

Figure 10.

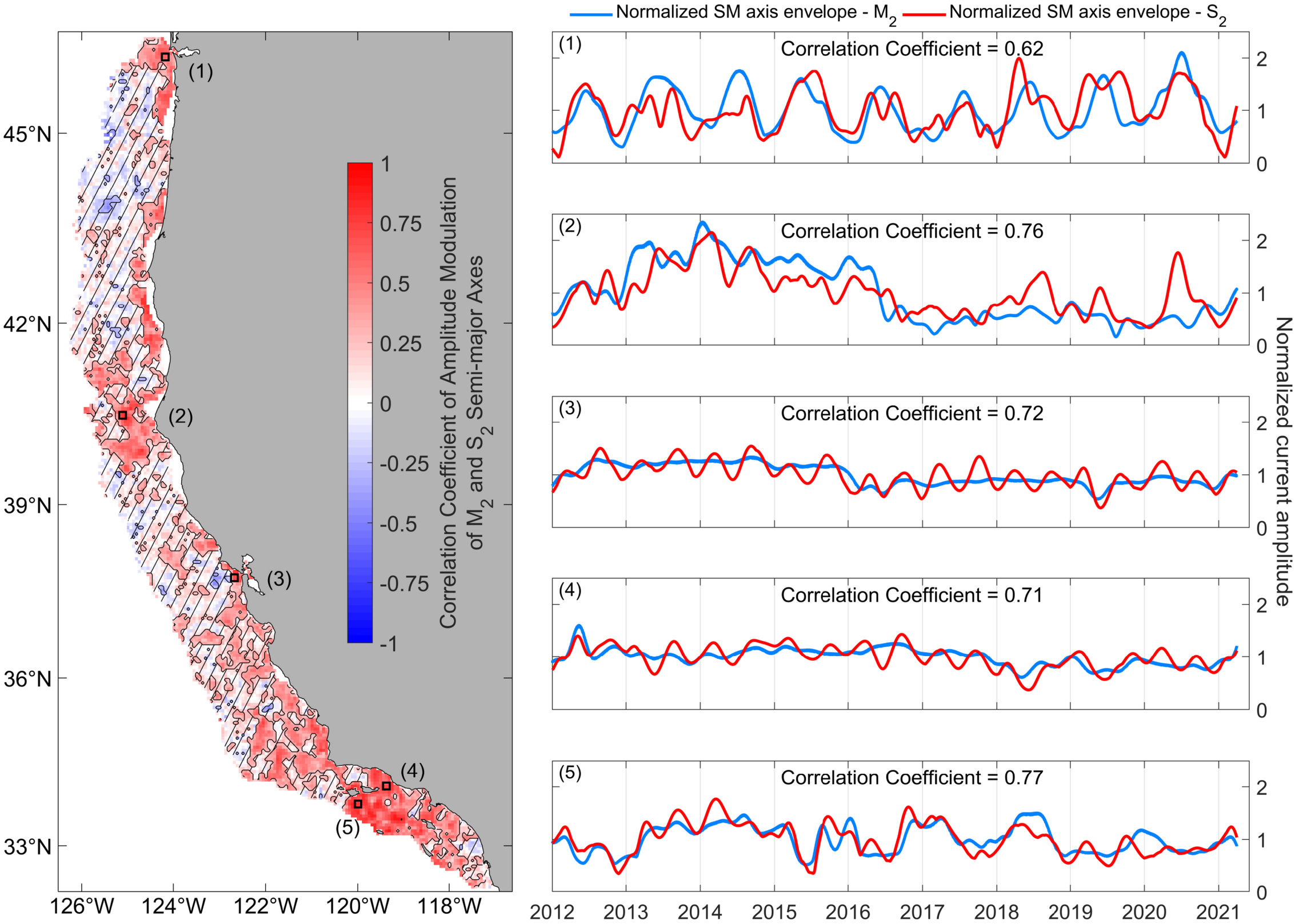
Normalized SM axis envelope - M2
Normalized SM axis envelope - S2
(1)
Correlation Coefficient = 0.62
(2)
Correlation Coefficient = 0.76
(3)
Correlation Coefficient = 0.72
(4)
Correlation Coefficient = 0.71
(5)
Correlation Coefficient = 0.77
Normalized current amplitude
Correlation Coefficient of Amplitude Modulation of M2 and S2 Semi-major Axes
1
0.75
0.5
0.25
0
-0.25
-0.5
-0.75
-1
45°N
42°N
39°N
36°N
33°N
126°W
124°W
122°W
120°W
118°W
2012
2013
2014
2015
2016
2017
2018
2019
2020
2021